# Green Chemistry

Accepted Manuscript


This is an *Accepted Manuscript*, which has been through the Royal Society of Chemistry peer review process and has been accepted for publication.

*Accepted Manuscripts* are published online shortly after acceptance, before technical editing, formatting and proof reading. Using this free service, authors can make their results available to the community, in citable form, before we publish the edited article. We will replace this *Accepted Manuscript* with the edited and formatted *Advance Article* as soon as it is available.

You can find more information about *Accepted Manuscripts* in the Information for Authors.



ROYAL SOCIETY OF CHEMISTRY

www.rsc.org/greenchem

Journal Name Green Chemistry Dynamic Article Links ►

Cite this: DOI: 10.1039/c0xx00000x

www.rsc.org/xxxxxx

ARTICLE TYPE

# Hierarchical hollow nanostructured core@shell recyclable catalysts γ-$Fe_2O_3$@LDH@$Au_{25}$-*x* for highly efficient alcohol oxidation

Shuangtao Yin, Jin Li, and Hui Zhang*

***Received (in XXX, XXX) Xth XXXXXXXXX 20XX, Accepted Xth XXXXXXXXX 20XX***

**DOI: 10.1039/b000000x**

A series of honeycomb-like hierarchical hollow nanostructured magnetic catalysts γ-$Fe_2O_3$@$M_3$Al-LDH@$Au_{25}$-*x* (*x* means determined mass of gold in wt%) have been successfully fabricated by a modified electrostatic adsorption of water-soluble captopril-capped $Au_{25}$ nanoclusters ($Au_{25}Capt_{18}$) on preprepared magnetic supports $Fe_3O_4$@$M_3$Al-LDH (M=Ni, Mg or Cu/Mg(0.5/2.5), LDH: layered double hydroxide) followed by proper calcinations. Characterization results show that the low Au loading samples γ-$Fe_2O_3$@$Ni_3$Al-LDH@$Au_{25}$-*x* (*x*=0.053, 0.11) show nearly atomic precise $Au_{25}$ nanoclusters ($Au_{25}$NCs) (~1.4 ± 0.3 – 1.9 ± 0.6 nm) dispersed on the surface of $Ni_3$Al-LDH shell, while the catalysts γ-$Fe_2O_3$@$M_3$Al-LDH@$Au_{25}$-*x* (*x*~0.2) display slightly aggregated $Au_{25}$NCs on the shell LDH with the size of ~3.0 ± 1.3, 3.3 ± 1.2 and 4.2 ± 1.5 nm for Ni-, Mg-, and CuMg-based catalyst, respectively, related to varied synergy between $Au_{25}$NCs and magnetic LDH supports at a little higher Au loadings. All the γ-$Fe_2O_3$@$M_3$Al-LDH@$Au_{25}$-*x* catalysts exhibit much higher catalytic activity for the oxidation of 1-phenylethanol under atmospheric $O_2$ without basic additives in toluene than $Fe_3O_4$@$Mg_3$Al-LDH@Au by traditional deposition-precipitation method. The catalyst γ-$Fe_2O_3$@$Ni_3$Al-LDH@$Au_{25}$-*x* presents even higher alcohol oxidation activity than γ-$Fe_2O_3$@$Mg_3$Al-LDH@$Au_{25}$-0.21 and γ-$Fe_2O_3$@$Cu_{0.5}Mg_{2.5}$Al-LDH@$Au_{25}$-0.2, and particularly, γ-$Fe_2O_3$@$Ni_3$Al-LDH@$Au_{25}$-0.053 exhibits the highest activity (TOF: 112498 $h^{-1}$) for the aerobic oxidation of 1-phenylethanol under solvent-free conditions and can be applied for a variety of alcohols, being mainly attributed to its nearly atomic precise $Au_{25}$NCs and remarkable $Au_{25}$NCs – LDH – magnetic core three-phase synergetic interaction along with its abundant Ni-OH sites. Moreover, the γ-$Fe_2O_3$@$Ni_3$Al-LDH@$Au_{25}$-0.053 can be easily separated by simply applying an external magnetic field and reused more than ten runs without significant loss of activity, rendering the magnetic catalysts long-term stability. These observations make the $Fe_3O_4$@LDH a universal green platform to support other noble or nonprecious metal nanoparticles by using metal nanocluster precursor method to construct desired metal-loaded ecofriendly catalysts that can be applied in a broad range of heterogeneous catalysis processes.

## Introduction

As one of the most fundamental transformation in organic synthesis, selective oxidation of alcohols attracts increasing research interest because of their corresponding products, i.e., carbonyl compounds are the important raw materials for the synthesis of fine chemicals.[1-3] During the past decade, it has been revealed that the supported noble metal nanoparticles (NPs) such as Pt[4], Ag[5], and Au[6,7] could efficiently catalyse the oxidation of alcohols. Particularly, Corma *et al.*[6] reported Au/$CeO_2$-nano catalyst exploring the combination effects of small-size Au (<5 nm) and nanoparticle $CeO_2$ (~5 nm) by a deposition-precipitation method, which turned out to obtain highly active and selective catalysts for the oxidation of alcohols compared to the catalyst of gold deposited on commonly precipitated $CeO_2$, but the synthesis of the nano-$CeO_2$ is tedious. Prati *et al.*[7] demonstrated that Au/nNiO (Au: 3.58 ± 0.97 nm, nNiO: nanosized NiO, 3-5 nm) by a sol immobilization method was more active for the liquid phase oxidation of benzyl alcohol under $O_2$ atmosphere (0.3 MPa) than the gold loaded on commercial NiO (42 nm). However, for the nanosized catalyst, separation using physical methods such as filtration or centrifugation, becomes a more difficult and time-wasting procedure. Thus from the view of green chemistry, development of highly active and easily recyclable catalysts has become significantly crucial. Therefore, magnetically recoverable nanocatalysts have received increasing attention in recent years because the minimization in achieving separations can result in significant economical and environmental benefits.[8-13]

With regard to the magnetically recyclable nanocatalysts, core@shell structural catalysts, combining the properties of magnetic core with the functionalized shell, have been widely used in the oxidation and reduction reactions.[10-15] Chen *et al.*[10] reported a core@shell $SiO_2$-coated Au-functionalized catalyst $Fe_3O_4$@$SiO_2$-Au with Au NPs of ~5 nm generated by *in situ* reduction of trivalent Au ion by bivalent Sn ion in solution and then linked to the surface of $Fe_3O_4$@$SiO_2$, which showed high catalytic activity in reduction of 4-nitro-phenol by $NaBH_4$ in water and good recovery efficiency at least for six consecutive cycles by simple magnetic separation. Xu *et al.*[11] prepared a multi-carboxylic hyperbranched polyglycerol-grafted $SiO_2$-coated iron oxide hybrid support ($Fe_3O_4$/$SiO_2$/HPG) followed directly growing Au NPs by using grafted HPGs as templates with nearly monodisperse sizes (6.0 ± 0.6 nm) and high Au loading. The $Fe_3O_4$/$SiO_2$/HPG-Au showed high catalytic activity for oxidation of alcohols with additive $K_2CO_3$ which unavoidably leads to corrosion and waste base treatment. Our group[12] have first

reported a facile one-step synthesis of honeycomb-like hierarchical core@shell structural superparamagnetic support $Fe_3O_4$@$Mg_3Al$-LDH (LDH: layered double hydroxide) followed loading Au NPs (~7.0 nm) by DP method affording high alcohol oxidation activity without basic additives under atmospheric $O_2$, which is more ecofriendly and greener than stoichiometric oxidation with a metal-involving inorganic oxidant dichromate or permanganate. However, the mean sizes of Au NPs in all these magnetic catalysts are larger than 2 nm, which significantly limit further enhancement of the catalytic activity of gold catalysts. It is noted that Goodman *et al.*[16] have prepared Au/$TiO_2$ catalyst in ultrahigh vacuum to investigate the unusual size-dependence of the low-temperature catalytic oxidation of carbon monoxide. The results indicated that the catalytic activity steeply increases with decreasing mean Au NPs' sizes from 4.0 nm to 3.5 nm, but oppositely reduces when the mean Au NPs' size below 3.5 nm because a metal-to-nonmetal transition occurs as the cluster size is reduced below 3.5 by 1.0 $nm^2$ (3.5 nm in diameter and 1.0 nm in height; 300 atoms per cluster). Wang *et al.*[17] prepared Au/hydrotalcite catalysts with mean Au NPs' sizes in 2.1-21 nm by DP route and studied their oxidant-free dehydrogenation properties of benzyl alcohol, showing that the activity is increased slightly with Au NPs reducing from 12 nm to ~4 nm while increased steeply as the mean Au NPs' size further reduced to 2.1 nm. Clearly, it is hard to obtain Au NPs below 2 nm on traditional loading methods such as sol immobilization, DP route and in situ reduction.[6,7,11-13,16-18] Thus, it is highly desired for further reduced size of Au NPs upon improved method for greatly improved alcohol oxidation activity and the practical applications.

Au nanoclusters (AuNCs) with defined atomic compositions and structures constitute a new class of materials and their sizes typically range from subnanometer to approximately 2 nm, attracting extensive attention as catalysts because of the obvious enhancement of catalystic activities with ultrafine AuNCs and structure-property correlation.[19-22] In our previous work, we first reported LDH loaded Au nanocluster catalysts with glutathione-capped AuNCs for alcohol oxidation and found AuNCs/$Ni_3Al$-LDH giving the highest 1-phenylethanol oxidation activity under solvent-free conditions (TOF: 46500 $h^{-1}$).[23] However, the pristine AuNCs and those in AuNCs/LDH catalysts show the average sizes of 1.5 ± 0.5 – 2.0 ± 0.7 nm, obviously larger than the critical size of $Au_{25}$ nanoclusters (~0.9 nm). Then in our most rencent report,[24] a series of $Ni_xAl$-LDH ($x$=2, 3, 4) loaded $Au_{25}$ clusters catalysts were obtained via a modified electrostatic adsorption of captopril-capped $Au_{25}Capt_{18}$ onto predispersed LDH, and found that nearly atomic precise $Au_{25}$/$Ni_3Al$-LDH (0.9 ± 0.2 nm) shows extrodinarily high activity (TOF: 118500 $h^{-1}$) for selective oxidation of 1-phenylethanol under no base additives and solvent-free conditions. However, considering the difficulties and time-consuming of the catalyst separation by traditional filtering or centrfuging process and highly efficient usage of Au catalyst, it is highly desirable to fabricate atomically precise recyclable nano-Au catalysts by Au nanoclusters precursor method. Meanwhile, the hollow nano-/microstructures recently stand for one of the fastest growing areas of materials science upon their distinct low effective density, high surface area, and potential applications.[25] Therefore, it is necessary to prepare hierarchical hollow magnetic core@shell nanostructure loaded ultrafine $Au_{25}$NCs for highly efficient catalytic oxidation of alcohols.

Herein, a series of honeycomb-like hierarchical hollow nanostructured magnetic catalysts γ-$Fe_2O_3$@$M_3Al$-LDH@$Au_{25}$-$x$ ($x$ refers to mass of $Au_{25}$ nanoclusters in wt%) with nearly atomic precise Au clusters have been carefully fabricated by a modified electrostatic adsorption of atomically precise captopril-capped $Au_{25}$ nanoclusters on preprepared core@shell magnetic supports $Fe_3O_4$@$M_3Al$-LDH (M=Ni, Mg or Cu/Mg (0.5/2.5)) and systematically characterized. We deeply study the size-loading correlation of $Au_{25}$NCs, the electron modification by LDH shell, and the influence of the compositions of magnetic supports on alcoho1 oxidation and shed new light on the $Au_{25}$NCs – magnetic supports synergetic effect. The γ-$Fe_2O_3$@$Ni_3Al$-LDH@$Au_{25}$-0.053 (1.4 ± 0.3 nm) exhibits the highest activity (TOF: 112498 $h^{-1}$) for the aerobic oxidation of 1-phenylethanol by $O_2$ under no base additives and solvent-free conditions. The reaction rate constant ($k$), apparent activation energy ($E_a$) and reaction mechanism of 1-phenylethanol oxidation over the magnetic catalysts were determined and discussed. Magnetic separation and recycling studies were conducted also.

## Experimental details

All of the chemicals were commercially available and used without further purification. Tetrachloauric (III) acid ($HAuCl_4 \cdot 4H_2O$, >99.9%, AR) and sodium borohydride (99.5%, AR) were supplied from Sinopharm Chemical Reagent Co., Ltd. Captopril ($C_9H_{15}NO_3S$, 99%, AR) was purchased from Changzhou Pharmaceutical Factory. Methanol ($CH_3OH$, ⩾99.9%, HPLC) was purchased from Tianjin Shield Specialty Chemical Ltd. Co. All of the substrate alcohols (AR) were purchased from Aladdin. The deionized water with the resistivity of >18.25 MΩ was used in the present study.

### Preparation of magnetic suppport $Fe_3O_4$@LDH

$Fe_3O_4$ submicrospheres (~530 nm) were prepared by using a solvothermal method as previously reported.[26] Then, the $Fe_3O_4$ powder of 1.0 g were dispersed in a 100 mL of deionized water under ultrasonically agitating for 15 min to obtain an uniform suspension. A 100 mL of aq. solution containing $Na_2CO_3$ (0.006 mol) and NaOH (0.02 mol) was added dropwise into the suspension until pH=10. Then, another aq. solution (100 mL) with $Ni(NO_3)_2 \cdot 6H_2O$ (0.009 mol) or $Mg(NO_3)_2 \cdot 6H_2O$ (0.009 mol) and $Al(NO_3)_3 \cdot 9H_2O$ (0.003 mol) was added dropwise into the above suspension under vigorous stirring at constant pH of 10 maintained by simultaneous addition of alkaline solution. The obtained slurry was aged at room temperature for 15 min. The resultant was separated by using a magnet (0.15 T), washed by deionized water for several times, then dried at 60 ºC for 24 h giving black support $Fe_3O_4$@$Ni_3Al$-LDH or $Fe_3O_4$@$Mg_3Al$-LDH.

The other support $Fe_3O_4$@$Cu_{0.5}Mg_{2.5}Al$-LDH was prepared according to our previous work.[13] In detail, 1.0 g $Fe_3O_4$ sample was dispersed into a 100 mL methanol/water solution ($V_{methanol}$/$V_{water}$=1:1) under ultrasonically agitating for 15 minutes to obtain a uniform suspension. A 200 mL mixed alkaline solution containing NaOH (0.04 mol) and $Na_2CO_3$ (0.012 mol) was added dropwise to above suspension until pH~10 and maintained there for 5 min. Then, another 100 mL of mixed salt solution

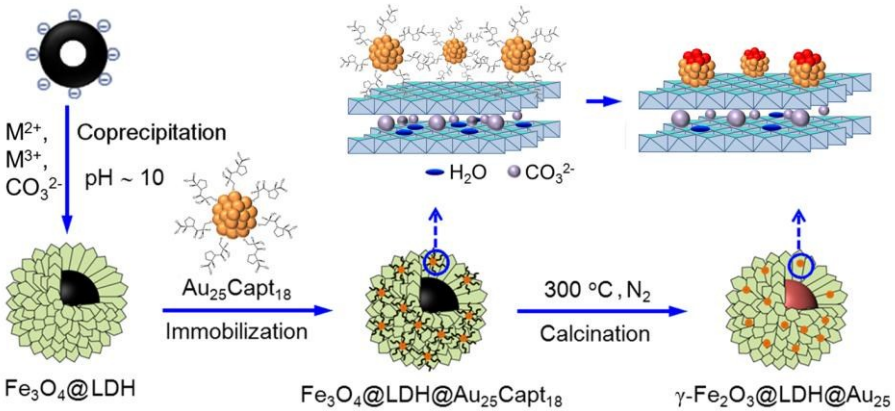


**Scheme 1** The synthetic strategy of the hierarchical hollow nanostructured magnetic catalysts γ-$Fe_2O_3$@$M_3$Al-LDH@$Au_{25}$-*x*.

containing $Cu(NO_3)_2 \cdot 3H_2O$ (0.0015 mol), $Mg(NO_3)_2 \cdot 6H_2O$ (0.0075 mol) and of $Al(NO_3)_3 \cdot 9H_2O$ (0.003 mol) was added dropwise to the above suspension while vigorously stirring at a constant pH~10 maintained by simultaneously adding alkaline solution. The resulting slurry was aged for 24 h in 60 ºC water bath while vigorously stirring. The resultant was separated using a magnet and thoroughly washed with deionized water and alcohol several times, and dried at 60 ºC overnight giving the product $Fe_3O_4$@$Cu_{0.5}Mg_{2.5}$Al-LDH.

**Preparation of the magnetic catalyst.**

The water-soluble captopril-capped $Au_{25}$ clusters ($Au_{25}Capt_{18}$) was synthesized by a size-focusing synthetic methodology according to the reference from Jin *et al*.[27] Typically, 8.23 mL $HAuCl_4 \cdot 4H_2O$ (10 mg/mL in methanol) was added to 1.77 mL methanol in a 25 mL single-necked flask while vigorously stirring at 25ºC. Then, TOABr (126.8 mg) was added to the flask and the solution color changes from yellow-orange to deep red. After 20 min, captopril (217.2 mg, dissolved in 5 mL methanol) was rapidly injected into the reaction mixture under stirring. The solution color quickly changed to white. After 30 min, an aq. solution of 5 mL of $NaBH_4$ (75.6 mg, dissolved in 5 mL of ice cold water) was rapidly added to the reaction mixture under vigorous stirring. The solution color immediately turned to brown-black. The reaction was allowed to proceed for 8 h and then the reaction mixture was centrifuged (5000 r/min, 20 min) to remove unreacted, insoluble Au(I):Capt intermediate complexes. The supernatant was collected and concentrated by rotary evaporation (30 ºC, 20 min). The brown-black products were precipitated by adding ethanol(20 mL) to the solution and standing overnight, then dried in vacuum at 30 ºC to give the raw product. Then, the raw product was extracted with minimum amounts of methanol several times, then precipitated again by adding ethanol (30 mL) and centrifuging (3000 r/min, 10 min) to obtain brown-blackish precipitate and dried at 30 ºC in vacuum overnight giving brown-blackish product $Au_{25}Capt_{18}$.

Then, the magnetic catalysts were prepared by a modified electrostatic adsorption method.[24] In detail, 1.25 g $Fe_3O_4$@$M_3$Al-LDH(M=Ni, Mg or Cu/Mg(0.5/2.5)) support was dispersed into 50 mL deionized water (pH=7.98, 7.83, 7.71). Then, 13.55 mL of $Au_{25}Capt_{18}$ solution (0.1471 mg/mL, pH=6.89) was added into the above suspension under vigorous stirring for 15 min at room temperature. Then the mixture was separated using a magnet and dried at 60 ºC overnight giving the black catalyst precursors $Fe_3O_4$@$M_3$Al-LDH@$Au_{25}Capt_{18}$. Then, the precursors were calcined at 300 ºC for 2 h under $N_2$ flowing giving the brick-red catalyst γ-$Fe_2O_3$@$M_3$Al-LDH@$Au_{25}$-*x* (*x*~0.2, x refers to the Au loading in wt% upon ICP data). Similarly, γ-$Fe_2O_3$@$Ni_3$Al-LDH@$Au_{25}$-0.11 and γ-$Fe_2O_3$@$Ni_3$Al-LDH@$Au_{25}$-0.053 were prepared by adjusting the amount of $Au_{25}Capt_{18}$ solution as 6.76 mL and 3.38 mL in the same way, respectively. Scheme 1 depicts the design schematic of the γ-$Fe_2O_3$@$Ni_3$Al-LDH@$Au_{25}$ catalysts.

**Characterization**

The UV-vis spectra were obtained on a Shimadzu UV-2501PC spectrophotometer. Transmission electron microscopy (TEM) was carried out on a Hitachi H-800 transmission electron microscope with an accelerating voltage of 100 kV. High Resolution (HR)TEM was recorded on a JEM 2010 transmission electron microscope with an accelerating voltage of 200 kV. Scanning electron microscopy (SEM) along with element mapping were recorded on a Hitachi S-3500N apparatus at 20 kV. Scanning electron microscopy (SEM) results were obtained on a Zeiss Supra 55 field emission scanning electron microscopy using a 15 kV electron beam and 60 s acquisition time. Powder X-ray diffraction (XRD) data were taken on a Shimadzu XRD-6000 diffractometer using Cu Kα radiation (1.5418 Å, 40 kV, 30 mA). The samples, as unoriented powders, were step-scanned in steps of 0.02° (2θ) in the range of 3-70° using a count time of 4 s per step. The Raman spectra were recorded at room temperature on a Jobin Yvon Horiba Raman spectrometer model HR800 with an excitation wavelength of 785 nm with the laser power of 0.2 mW. Magnetic properties of the samples were measured on a Lake Shore 7410 vibrating sample magnetometer (VSM) at 298 K and 20 kOe applied magnetic field. The surface chemical composition of the catalyst was studied on a VG ESCALAB-250 X-ray photoelectron spectrometer at a base pressure in the analysis chamber of $2 \times 10^{-9}$ Pa using a standard Al Kα source (1486.6 eV). The binding energy scale was referenced to the C 1s line of aliphatic carbon contamination set at 285.0 eV. CO adsorption FT-IR studies were carried out on a Nicolet 380 instrument containing a controlled environment chamber equipped with $CaF_2$

windows. IR spectra were recorded by using wafers in the form of self-supporting pellets of the catalysts powder mounted in a homemade ceramic cell. Prior to measurements, the samples were first heated to 100 ℃ at a heating rate of 5 ℃/min in a flowing $N_2$ stream and kept for 1 h and then cooled to 50 ℃. The sample was scanned to get a background record, then exposed to a CO flow for 1 h. Subsequently the cell was purged with $N_2$ for 30 min. The IR spectra of CO adsorbed on Au catalyst were recorded in absorbance mode at 4 $cm^{-1}$ resolution by averaging 64 scans.

**Activity test**

The liquid-phase aerobic oxidation of 1-phenylethanol was performed using 25 mL three-necked round-bottle flask with a reflux condenser under magnetic stirring. The substrate (1 mmol), solvent (toluene, 5 mL) and catalyst (Au: 0.2 mol%) were mixed in the flask and then heated to reaction temperature with $O_2$ bubbling (20 mL/min) at atmospheric pressure. During the reaction, 0.2 mL aliquots were pipetted every 15 min, filtered and analyzed by GC (Agilent 7890A) equipped with a flame ionisation detector and an Agilent J&K HP-5 (5% phenyl polysiloxane, 30 m × 0.25 nm × 0.25 μm) capillary column. Biphenyl was used as an internal standard for quantitative analysis. The solvent-free oxidation of 1-phenylethanol was done as follow: 1-phenylethanol (100 mmol), catalyst (Au: $4.0 \times 10^{-4}$ mol%), reaction temperature (160 ºC). After the reaction, the catalyst was separated by external magnetic field and washed with toluene and dried at 60 ºC overnight.

**Recycling procedure**

After completion of the oxidation reaction, the catalyst was separated by an external magnetic field (NdFeB magnet of 0.15 T) followed by washing with toluene, the catalyst was then used directly in the next run without further purification.

## Results and discussion

**Synthesis of the catalysts by using $Au_{25}Capt_{18}$ precursor.**

Firstly, $Au_{25}Capt_{18}$ nanoclusters was successfully obtained upon FT-IR, UV-vis, and HRTEM data. The ligation of captopril in the form of the thiolate to the gold core was verified by the absence of IR band ν(S-H) at 2567 $cm^{-1}$ in $Au_{25}Capt_{18}$ (Fig. S1A, curve b).[28] The UV-vis spectrum of original solution of $Au_{25}Capt_{18}$ (Fig. 1A, curve a) shows an exponential-like decay from the UV region into the visible region while featured by a definite absence of surface plasmon resonance at ~520 nm for Au nanocrystals > 2 nm,[22,23] implying the ultrafine clusters of the obtained $Au_{25}Capt_{18}$ below 2.0 nm. Moreover, because of strong quantum size effects, $Au_{25}Capt_{18}$ nanocluster shows multiple molecule-like transitions in the optical spectrum with at least three distinct bands at 670, 450, and 400 nm. The excited state at 670 nm corresponds to a LUMO←HOMO transition, an essential intraband (sp←sp) transition, which can be viewed as a transition entirely due to the electronic and geometric structure of the $Au_{13}$ core.[29] The band at 450 nm arises from mixed intraband (sp←sp) and interband (sp←d) transitions, and the one at 400 nm arises principally from an interband transition (sp←d). Meanwhile, a broad shoulder at ~800 nm (spin-forbidden) is observed and the 400 nm band is less pronounced, implying that native $Au_{25}Capt_{18}$ clusters are indeed

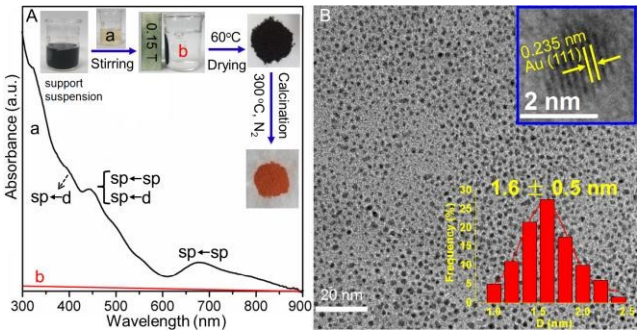


**Fig. 1** (A) UV-vis spectra of original water solution of $Au_{25}Capt_{18}$ (a) and supernatant solution after adsorption on support $Fe_3O_4$@$M_3$Al-LDH (b); (B) HRTEM of $Au_{25}Capt_{18}$ (inset is histogram of Au size distribution).

anionic.[30] The ESI-MS data further suggest the obtained gold clusters to be $Au_{25}Capt_{18}$ (Fig. S2). The XRD of $Au_{25}Capt_{18}$ (Fig. S3) shows a clear peak at 37.5º (111) and a very broad one at 64.5º, and the $D_{111}$ is tentatively estimated as 0.80 nm by the Debye-Scherrer equation ($D_{hkl} = 0.9\lambda/(\beta \cdot \cos\theta)$, where $\beta$ is the full width at half maximum (in rad.), and $\lambda$ is the wavelength), implying the ultrasmall size of $Au_{25}$NCs. The HRTEM image of $Au_{25}Capt_{18}$ (dispersed in water) (Fig. 1 B) reveals an average Au core size of 1.6 ± 0.5 nm (upon ~200 particles), consistent with the above UV-vis result.

During the synthesis process of catalysts, it was clearly seen that $Au_{25}Capt_{18}$ were adsorbed quickly onto the surface of magnetic supports (photos in Fig. 1A ), as verified by the colorless supernatant (Fig. 1A, curve b), probably via strong electrostatic attraction between the negatively charged $Au_{25}Capt_{18}$ originated from its carboxyl groups and the positively charged $M^{2+}/Al^{3+}$-LDH sheets, resulting in black catalyst precursor $Fe_3O_4$@$M_3$Al-LDH@$Au_{25}Capt_{18}$. As the TG plot of $Au_{25}Capt_{18}$ (Fig. S1B along with experiment) shows a constant weight loss of ~44% after 300 ºC, the catalyst precursors was subsequently calcined at 300 ºC for 2 h in notrogen flow to remove the ligands, resulting in the brick-red catalyst γ-$Fe_2O_3$@$M_3$Al-LDH@$Au_{25}$ (photo in Fig. 1A).

**The crystal structure and chemical composition.**

Fig. 2 shows the XRD patterns of γ-$Fe_2O_3$@$Ni_3$Al-LDH@$Au_{25}$-*x* catalysts, corresponding supports and $Fe_3O_4$. The $Fe_3O_4$ sample depicts sharp (220) (30.3º), (311) (35.5º), (400) (43.3º), (511) (57.4º) and (440) (63.1º) lines of the cubic magnetite phase (JCPDS 110614). The Scherrer dimension upon (311) line is 29.6 nm, close to the critical size of the bulk $Fe_3O_4$,[31] implying superparamagnetization property of the obtained $Fe_3O_4$. All the supports $Fe_3O_4$@$M_3$Al-LDH (M=Ni, Mg or Cu/Mg(0.5/2.5)) (Fig. 2$a_0$, $b_0$, $c_0$) present a series of weak but distinguishable (00*l*) lines at low 2θ angles and (110) lines at ~61.3º (enlarged region in Fig. 2) corresponding to typical hexagonal LDH phase,[12,32] and sharp (220), (311), (400), (511) and (440) lines of $Fe_3O_4$ phase, indicating the formation of well-defined $Fe_3O_4$@$M_3$Al-LDH composites. The intensity ratio of (110) to (003) lines ($I_{110}/I_{003}$), an indicative for oriented growth of LDH platelet-like crystals, is 0.60, 1.00 and 0.26 for $Fe_3O_4$@$Ni_3$Al-LDH, $Fe_3O_4$@$Mg_3$Al-LDH, $Fe_3O_4$@$Cu_{0.5}Mg_{2.5}$Al-LDH, respectively, which are obviously larger than pure $Ni_3$Al-LDH (0.5) (JCPDS 150087), $Mg_3$Al-LDH (0.26)[12], and CuMgAl-LDH (0.23)[13], suggesting an extremely

well-oriented growth of $M_3Al$-LDH with *a*,*b*-face vertical to the surface of the $Fe_3O_4$ core.[12,33,34] However, for the catalysts γ-$Fe_2O_3$@$Ni_3Al$-LDH@$Au_{25}$-*x*, the sharp lines of (220) (30.4°), (311) (35.6°), (400) (43.5°), (511) (57.4°) and (440) (63.1°) show slightly shift to higher angles compared with those of $Fe_3O_4$, which can be indexed to γ-$Fe_2O_3$[35] (JCPDS 391346), implying the possible phase transformation from initial $Fe_3O_4$ to γ-$Fe_2O_3$ occurred upon the loading of $Au_{25}Capt_{18}$ followed by calcinations since pure $Fe_3O_4$@LDH shows no phase transformation on the same calcinations. Raman spectra of a series of samples including the catalyst γ-$Fe_2O_3$@$Ni_3Al$-LDH@$Au_{25}$-0.053, corresponding support $Fe_3O_4$@$Ni_3Al$-LDH and precursor $Fe_3O_4$@$Ni_3Al$-LDH@$Au_{25}Capt_{18}$-0.053, and $Fe_3O_4$ core (Fig. S4) show that the catalyst possesses three broad structures at ca. 350, 508, and 710 $cm^{-1}$, which are typical characteristics of the maghemite,[36] while the support and precursor show the characteristics of pure $Fe_3O_4$ phase,[25] clearly indicating the occurrence of phase transformation from $Fe_3O_4$ to γ-$Fe_2O_3$ in the catalyst upon the loading of $Au_{25}Capt_{18}$ and calcinations. Although the basal spacings of the γ-$Fe_2O_3$@$M_3Al$-LDH@$Au_{25}$-*x* catalysts are reduced to 0.663-0.683 nm compared to $Fe_3O_4$@$M_3Al$-LDH supports (0.752-0.777 nm) (Table S1), probably due to the removal of interlayer water and partial $CO_3^{2-}$ ions, the (003) and (110) lines can be clearly seen in the enlarged patterns (Fig. 2), indicating the maintainance of LDH layer structures. Notably, the diffractions related to Au(111) cannot be detected, implying the ultrafine Au size of the catalysts.

The IR spectra of the catalysts γ-$Fe_2O_3$@$M_3Al$-LDH@$Au_{25}$-*x* and corresponding precursors and supports (Fig. S5) mainly show the typical IR bands of $CO_3^{2-}$-LDH phase.[32] All the precursors $Fe_3O_4$@$M_3Al$-LDH@$Au_{25}Capt_{18}$-*x* (Fig. S5(a'-c')) and supports $Fe_3O_4$@$M_3Al$-LDH (Fig. S5($a_0$-$c_0$)) show wide strong $\nu_{OH}$ band at ~3460 $cm^{-1}$ due to the -OH groups on the LDH layer, sharp $\nu_3$ bands at ~1370 $cm^{-1}$ to the interlayer $CO_3^{2-}$ ions,[32] $\delta_{H2O}$ at ~1638 $cm^{-1}$ from the hydroxyl deformation mode of interlayer water, and sharp $\nu_{Fe-O}$ band at 584 $cm^{-1}$ to the lattice mode of $Fe_3O_4$,[27,31] indicating the well-defined assembly of $CO_3^{2-}$-LDH phase and $Fe_3O_4$ phase. The precursors also show clear bands around 2932 $cm^{-1}$ due to $\nu_{C-H}$ of $CH_3$ and $CH_2$ groups from captopril ligands (Fig. S5(a'-c')). Then for the γ-$Fe_2O_3$@$M_3Al$-LDH@$Au_{25}$-*x* catalysts, these features except $\nu_{Fe-O}$ are clearly weakened due to the evaporation of interlayer water and partial $CO_3^{2-}$ anions via calcination, and nearly disappeared $\nu_{C-H}$ indicates the nearly complete removal of the ligand in hierarchical structure.[24] It is noted that all the samples involving $Ni_3Al$-LDH show relatively narrower $\nu_{OH}$ band than other two systems, suggesting that more ordered LDH layers may exist in γ-$Fe_2O_3$@$Ni_3Al$-LDH@$Au_{25}$-*x* catalysts.

**Morphology of the catalysts.**

Fig. 3 presents the SEM and HRTEM images of the catalysts γ-$Fe_2O_3$@$M_3Al$-LDH@$Au_{25}$-*x*, while those of supports and $Fe_3O_4$ are given in Fig. S6. From Fig. S6(a, b), it can be clearly seen that $Fe_3O_4$ nanospheres possess a smooth surface with narrow size distribution (~530 nm) and hollow interior with shell thickness of ~185 nm consisting of even small particles of ~30.6 nm. This unique hollow structure implies that the obtained $Fe_3O_4$ possesses

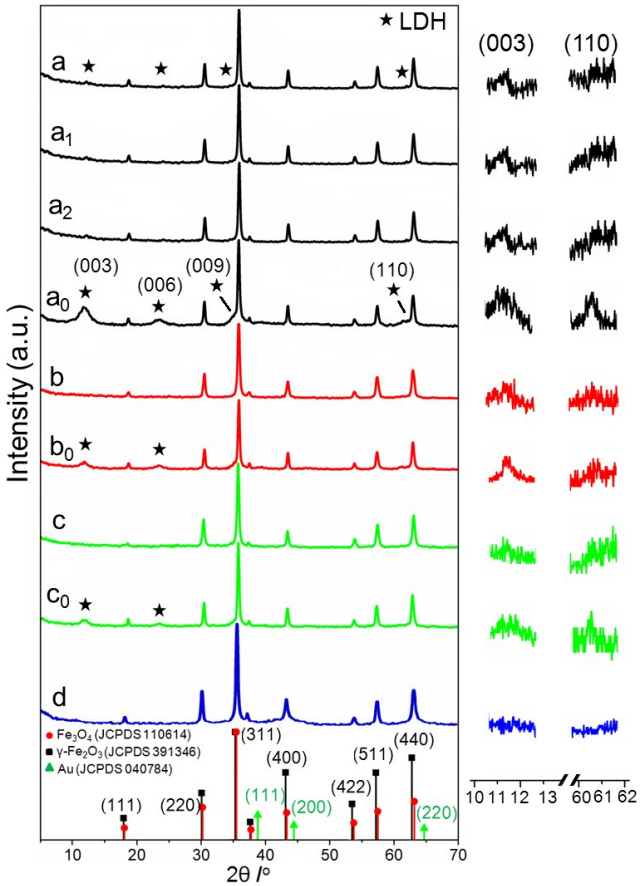


**Fig. 2** XRD patterns of the γ-$Fe_2O_3$@$Ni_3Al$-LDH@$Au_{25}$-*x* catalysts (*x* = 0.23 (a), 0.11($a_1$) and 0.053 ($a_2$), γ-$Fe_2O_3$@$Mg_3Al$-LDH@$Au_{25}$-0.21 (b), and γ-$Fe_2O_3$@$Cu_{0.5}Mg_{2.5}Al$-LDH@$Au_{25}$-0.2 (c), corresponding supports ($a_0$ −$c_0$) and $Fe_3O_4$ (d).

distinct low effective density and high surface area as BET analysis (experimental shown in SI) evidenced (11.8 $m^2\ g^{-1}$), which is much higher than the previously reported similar sized solid $Fe_3O_4$ spheres (5.4 $m^2\ g^{-1}$ and 2.2 $m^2\ g^{-1}$)[25,34]. After coating with $CO_3$-LDH (Fig. S6(c, e, g)), a honeycomb-like morphology with many voids of ~50 - 100 nm is clearly seen for $Fe_3O_4$@$M_3Al$-LDH supports. Interestingly, the $M_3Al$-LDH shell presents a marked preferred orientation with the *c*-axis parallel to and *ab*-face vertical to the surface of $Fe_3O_4$ cores. Specially, the shell LDH nanoplates of $Fe_3O_4$@$Ni_3Al$-LDH are seemingly more fine and dense than the $Fe_3O_4$@$Mg_3Al$-LDH and $Fe_3O_4$@$Cu_{0.5}Mg_{2.5}Al$-LDH. The TEM images of the $Fe_3O_4$@$M_3Al$-LDH supports (Fig. S6(d, f, h)) undoubtedly confirm the hollow core-shell structure with the $Fe_3O_4$ cores well-coated by a layer of LDH nanocrystallites. In detail, the $Ni_3Al$-LDH nanocrystal monolayers are formed as uniform ultrathin nanosheets with a thickness of ~11.7 nm and a width of ~70 nm, growing from the magnetite core to the outer surface and perpendicular to the core surface. It should be mentioned that this honeycomb-like morphology of the supports $Fe_3O_4$@$M_3Al$-LDH can finely avoid the aggregation of single LDH platelet-like nanoparticles as often occurred,[37] and facilitate the adsorption of active metal nanoparticles onto the exposed edge sites of the vertically cross-linked LDH nanoplates.

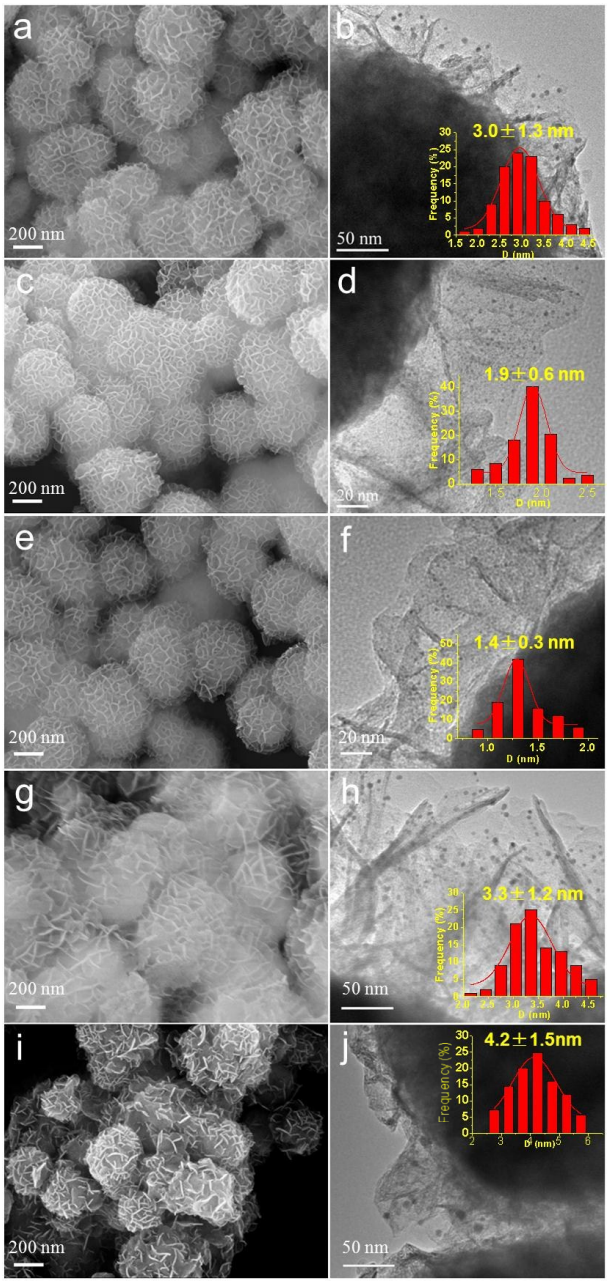


**Fig. 3** SEM and HRTEM of γ-$Fe_2O_3$@$Ni_3$Al-LDH@$Au_{25}$-*x* (*x* = 0.23 (a, b), 0.11(c, d) and 0.053 (e, f), γ-$Fe_2O_3$@$Mg_3$Al-LDH@$Au_{25}$-0.21 (g, h), γ-$Fe_2O_3$@$Cu_{0.5}Mg_{2.5}$Al-LDH@$Au_{25}$-0.2 (i, j) (insets, the size distributions).

Then, the SEM images of the γ-$Fe_2O_3$@$M_3$Al-LDH@$Au_{25}$-*x* catalysts (Fig. 3a, c, e, g, i) show well-maintained honeycomb-like morphology, suggesting considerably stable core-shell structures of the present γ-$Fe_2O_3$@$M_3$Al-LDH@$Au_{25}$-*x* catalysts probably resulted from the stronger interaction between $M_3$Al-LDH shell and magnetic core. As for the clearly detected looser honeycomb-like morphology along with larger voids for γ-$Fe_2O_3$@$Mg_3$Al-LDH@$Au_{25}$-0.21 and γ-$Fe_2O_3$@$Cu_{0.5}Mg_{2.5}$Al-LDH@$Au_{25}$-0.2, which might be due to their obviously larger and thicker LDH nanoplates on Mg- or CuMg-LDH layers (Table S1). This open network structures with wide voids may facilitate the accesibility of the reactants to the active sites, thus may specially improve the catalytic activity and stability of the $Au_{25}$NCs – LDH shell – magnetic core three-phase nanocomposite catalysts.

The HRTEM images of the γ-$Fe_2O_3$@$Ni_3$Al-LDH@$Au_{25}$-0.23 (Fig. 3b), γ-$Fe_2O_3$@$Mg_3$Al-LDH@$Au_{25}$-0.21 (Fig. 3h), γ-$Fe_2O_3$@$Cu_{0.5}Mg_{2.5}$Al-LDH@$Au_{25}$-0.2 (Fig. 3j) catalysts display highly dispersed $Au_{25}$NCs on the edges of shell LDH nanoplates with an average Au core size of 3.0±1.3, 3.3±1.2, and 4.2±1.5 nm, respectively, exhibiting an obviously increased mean size, compared to pure $Au_{25}Capt_{18}$ (1.6 ±0.5 nm), probably due to the sintering function of adjacent $Au_{25}$NCs. However, it could be envisioned that besides the commonly occurred sintering of adjacent $Au_{25}$NCs, there might be another possible reason, perhaps the interaction between the ultrafine $Au_{25}$NCs and $Fe_3O_4$@$M_3$Al-LDH which inevitably lead to the formation of large $Au_{25}$NCs during the calcining step and thus might enhance the stability of the atom packing structure of $Au_{25}$NCs during the catalytic process in favor of a better catalytic performance of the γ-$Fe_2O_3$@$M_3$Al-LDH@$Au_{25}$-*x* catalysts.

Tsukuda *et al.*[38] have ever reported the $Au_{25}$-HAP (0.2-0.5 wt%) catalysts and found the strong interaction between $Au_{25}$ and HAP, which led to the size-increased Au clusters from 1.0 of $Au_{25}SG_{18}$ to 1.4 nm of $Au_{25}$-HAP, but believed that the sintering of Au nanoclusters did not function during the calcination in their work. While Zhang *et al.*[23] found that the Coulomb repulsion among the carboxyl groups of the adsorbed glutathione-AuNCs and the synergetic effect between AuNCs and $Mg_3$Al-LDH co-lead to the approximately uniform dispersity and the formation of a little larger AuNCs on the LDH supports during calcination.

Then in the present work, we note that even the low $Au_{25}$ loading samples γ-$Fe_2O_3$@$Ni_3$Al-LDH@$Au_{25}$-*x* (*x*=0.11, 0.053) (Fig. 3(d, f) still show slightly increased or comparable average Au core sizes of 1.9 ±0.6 or 1.4 ±0.3 nm to pure $Au_{25}Capt_{18}$, though they shows ultrafine $Au_{25}$NCs compared to high loading sample γ-$Fe_2O_3$@$Ni_3$Al-LDH@$Au_{25}$-0.23. Also, the SEM mapping of γ-$Fe_2O_3$@$Ni_3$Al-LDH@$Au_{25}$-0.053 (Fig. S7) clearly indicates that the elements Ni, Al and Au are uniformly dispersed in the catalyst. Apparently, these results indicate that the sintering interaction of adjacent $Au_{25}$NCs function during the calcinations for the γ-$Fe_2O_3$@$Ni_3$Al-LDH@$Au_{25}$-*x* catalysts, in which the synergetic interaction between the nearly atomic precise $Au_{25}$NCs and magnetic LDH support plays more predominant role on the size of $Au_{25}$NCs especially with low gold loading samples.

Furthermore, the high-magnified HRTEM images of the γ-$Fe_2O_3$@$M_3$Al-LDH@$Au_{25}$-*x* catalysts clearly show that all the catalysts exhibit both cubic Au phase with (111) lattice fringes and hexagonal LDH phase with (015) lattice fringes. However, the obvious sintering of vicinal Au clusters can be clearly observed for γ-$Fe_2O_3$@$M_3$Al-LDH@$Au_{25}$-*x* (~0.2) leading to its relatively larger Au core size (Fig. 4(a, b, c)). While γ-$Fe_2O_3$@$Ni_3$Al-LDH@$Au_{25}$-0.053 (Fig. 4$a_2$) shows ultrafine Au core sizes < 2 nm. It is noted that for all the catalysts, the Au (111) planes parallel to the $Ni_3$Al-LDH (015) planes, attributing to their small mismatch of lattice constants facilitating the epitaxial orientation.[39] Considering the similar Au core size (~1.4 nm) in this catalyst to pure $Au_{25}Capt_{18}$, we infer that the Au clusters are more likely to be epitaxially diffused onto the surface of the magnetic supports forming ultrafine $Au_{25}$NCs. Noted that the low Au loading samples γ-$Fe_2O_3$@$Ni_3$Al-LDH@$Au_{25}$-*x* (*x* = 0.11, 0.053) clearly show more irregular ultrafine gold clusters

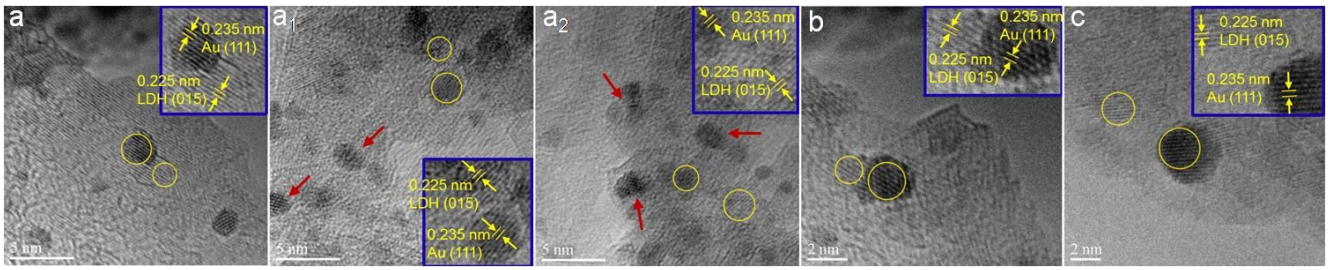


**Fig. 4** HRTEM images of the catalysts γ-$Fe_2O_3$@$Ni_3$Al-LDH@$Au_{25}$-*x* (*x* = 0.23 (a), 0.11 ($a_1$), and 0.053 ($a_2$)), γ-$Fe_2O_3$@$Mg_3$Al-LDH@$Au_{25}$-0.21 (b), and γ-$Fe_2O_3$@$Cu_{0.5}Mg_{2.5}$Al-LDH@$Au_{25}$-0.2 (c).

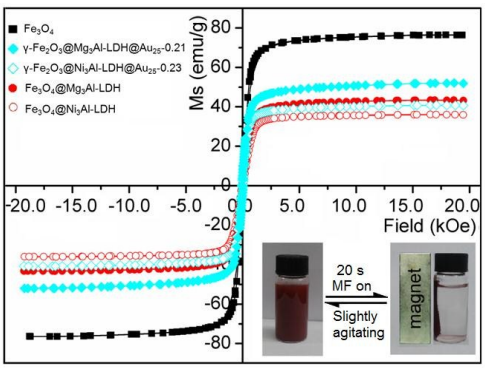


**Fig. 5** Room temperature magnetization plots of the catalysts γ-$Fe_2O_3$@$M_3$Al-LDH@$Au_{25}$-*x*, corresponding supports and $Fe_3O_4$ core.

(marked by blue arrows). These phenomena seemingly suggest the possible existence of strong adhesion among the $Au_{25}$NCs, the shell LDH and the magnetic core.

**The magnetization analysis.**

Fig. 5 shows the magnetization curves of the catalysts compared with corresponding supports and $Fe_3O_4$ core. All the samples present superparamagnetic properties. The magnetic saturation (Ms) values of the supports $Fe_3O_4$@$Mg_3$Al-LDH and $Fe_3O_4$@$Ni_3$Al-LDH are decreased to 38.6 and 35.4 emu $g^{-1}$, respectively, compared to $Fe_3O_4$ (76.6 emu $g^{-1}$), mainly due to the diamagnetic LDH shell coated on the surface of $Fe_3O_4$ core.[12] However, the slightly enhanced Ms values of γ-$Fe_2O_3$@$Mg_3$Al-LDH@$Au_{25}$-0.21 (51.9 emu $g^{-1}$) and γ-$Fe_2O_3$@$Ni_3$Al-LDH@$Au_{25}$-0.23 (40.8 emu $g^{-1}$) compared to corresponding supports can be attributed to the reduction of the diamagnetic hydrogen bond, $CO_3^{2-}$ and $H_2O$[12] and the $Fe_3O_4$→γ-$Fe_2O_3$ phase transition[40] upon calcinations. When the magnetic catalysts undergo strong magnetization, the catalysts particles can be magnetized and therefore can afford efficient magnetic separation with an external magnetic field (Fig. 5, inset).

**The oxidation activities of the catalysts.**

Table 1 presents the catalytic activities of the various magnetic catalysts in oxidation of 1-phenylethanol, a typical secondary alcohol, to acetophenone with atmospheric $O_2$ without basic additivies. Initially, the tests were conducted at 80 °C in toluene (Table 1, entries 1-5). The pure support $Fe_3O_4$@$Ni_3$Al-LDH and $Fe_3O_4$ core show very low conversion for 1-phenylethanol of 1.1% and 5.7%, respectively (Table 1, entries 15 and 16), confirming that gold clusters are the active surface for the alcohol oxidation reaction as previously reported.[12,17,41,42] The pristine $Au_{25}Capt_{18}$ clusters also fail to show any activity being ascribed to the presence of captopril ligands which significantly inhibit the accessibility of reactants to the surface of gold clusters. However, all γ-$Fe_2O_3$@$M_3$Al-LDH@$Au_{25}$-*x* catalysts exhibit much higher catalytic activity for the aerobic oxidation of 1-phenylethanol in toluene than $Fe_3O_4$@$Mg_3$Al-LDH@Au(DP) by traditional DP method without basic additives,[12] though the catalyst such as γ-$Fe_2O_3$@$Ni_3$Al-LDH@$Au_{25}$-0.053 gives quite low conversion (8.1%) in the absence of $O_2$ (Table 1, entry 10). The γ-$Fe_2O_3$@$Ni_3$Al-LDH@$Au_{25}$-0.23 shows much higher alcohol oxidation activity with TOF of 319.3 $h^{-1}$ than γ-$Fe_2O_3$@$Mg_3$Al-LDH@$Au_{25}$-0.21 (237.7 $h^{-1}$) and γ-$Fe_2O_3$@$Cu_{0.5}Mg_{2.5}$Al-LDH@$Au_{25}$ (128.7 $h^{-1}$) (Table 1, entries 1, 6 and 7), which may be associated with the finely and densely honeycomb-like morphology of γ-$Fe_2O_3$@$Ni_3$Al-LDH@$Au_{25}$-0.23 and possibly stronger gold-support interactions (later confirmed).

Furthermore, the low gold loading catalysts γ-$Fe_2O_3$@$Ni_3$Al-LDH@$Au_{25}$-0.11 (562.8 $h^{-1}$) and γ-$Fe_2O_3$@$Ni_3$Al-LDH@$Au_{25}$-0.053 (1297 $h^{-1}$) (Table 1, entries 2 and 3) present extraordinarily higher alcohol oxidation activity than γ-$Fe_2O_3$@$Ni_3$Al-LDH@$Au_{25}$-0.23, which may be ascribed to the nearly atomic precise $Au_{25}$NCs of the formers. Meanwhile, γ-$Fe_2O_3$@$Ni_3$Al-LDH@$Au_{25}$-0.053 also shows 13% higher activity than ultrafine AuNCs@$Ni_3$Al-LDH-0.22[23] (Table 1, entries 5 and 13) and comparable activity to nearly atomic precise $Au_{25}$/$Ni_3$Al-LDH[24] in the same conditions (Table 1, entries 4 and 11).

These results clearly indicate that the aerobic oxidation reactivity of 1-phenylethanol depends strongly on the sizes of $Au_{25}$NCs, and the smaller the gold clusters, the more coordinatively unsaturated gold atoms, the higher the 1-phenylethanol conversion, though there is no size-dependence for selectivity of the ketone products (all reach 99%). This size effect can be predominantly attributed to the ultrafine nearly atomic precise $Au_{25}$NCs on the present magnetic catalysts, though it is somewhat similar to Wang's report on Au/HT catalysts showing steeply increased TOF from ~300 to ~800 $h^{-1}$ with Au particle sizes reduced from 4 to 2.0 nm for oxidant-free dehydrogenation of benzyl alcohol.[17]

Moreover, the γ-$Fe_2O_3$@$Ni_3$Al-LDH@$Au_{25}$-0.053 exhibits extremely high activity for aerobic oxidation of 1-phenylethanol under solvent-free conditions (Table 1, entry 9) with TOF of 112498 $h^{-1}$ and 22.4% yield of acetophenone at 160 °C. This

**Table 1** Aerobic oxidation of 1-phenylethanol over the various γ-$Fe_2O_3$@$M_3$Al-LDH@$Au_{25}$-*x* catalysts.[a]

| Entry | Catalysts | Au/wt% (ICP) | $D_{Au}$/nm (TEM) | t / h | Conv. /% | Sel. /% | TOF / $h^{-1}$ [b] | Ref. |
|---|---|---|---|---|---|---|---|---|
| 1 | γ-$Fe_2O_3$@$Ni_3$Al-LDH@$Au_{25}$-0.23 | 0.23 | 3.0 ± 1.3 | 1.5 | 95.8 | > 99 | 319.3 | This work |
| 2[c] | γ-$Fe_2O_3$@$Ni_3$Al-LDH@$Au_{25}$-0.11 | 0.11 | 1.9 ± 0.6 | 1.75 | 98.5 | >99 | 562.8 | This work |
| 3[c] | γ-$Fe_2O_3$@$Ni_3$Al-LDH@$Au_{25}$-0.053 | 0.053 | 1.4 ± 0.3 | 0.75 | 97.3 | >99 | 1297 | This work |
| 4[d] | γ-$Fe_2O_3$@$Ni_3$Al-LDH@$Au_{25}$-0.053 | 0.053 | 1.4 ± 0.3 | 1 | 56.1 | >99 | 5610 | This work |
| 5[e] | γ-$Fe_2O_3$@$Ni_3$Al-LDH@$Au_{25}$-0.053 | 0.053 | 1.4 ± 0.3 | 1 | 96.4 | >99 | 6427 | This work |
| 6 | γ-$Fe_2O_3$@$Mg_3$Al-LDH@$Au_{25}$-0.21 | 0.21 | 3.3 ± 1.2 | 2 | 95.1 | > 99 | 237.7 | This work |
| 7 | γ-$Fe_2O_3$@$Cu_{0.5}Mg_{2.5}$Al-LDH@$Au_{25}$-0.2 | 0.20 | 4.2 ± 1.5 | 2 | 51.5 | >99 | 128.7 | This work |
| 8[f] | γ-$Fe_2O_3$@$Ni_3$Al-LDH@$Au_{25}$-0.23 | 0.23 | 3.0 ±1.3 | 0.5 | 18 | >99 | 90000 | This work |
| 9[f] | γ-$Fe_2O_3$@$Ni_3$Al-LDH@$Au_{25}$-0.053 | 0.053 | 1.4 ± 0.3 | 0.5 | 22.4 | >99 | 112498 | This work |
| 10[g] | γ-$Fe_2O_3$@$Ni_3$Al-LDH@$Au_{25}$-0.053 | 0.053 | 1.4 ± 0.3 | 1 | 8.1 | >99 | 810 | This work |
| 11[d] | $Au_{25}$/$Ni_3$Al-LDH | 0.191 | 0.9 ± 0.2 | 1 | 58.7 | >99 | 5870 | Ref. 24 |
| 12[f] | $Au_{25}$/$Ni_3$Al-LDH | 0.191 | 0.9 ± 0.2 | 0.5 | 23.68 | >99 | 118400 | Ref. 24 |
| 13[e] | AuNCs@$Ni_3$Al-LDH-0.22 | 0.22 | 1.5 ± 0.5 | 1 | 85.3 | >99 | 5687 | Ref. 23 |
| 14[f] | AuNCs@$Ni_3$Al-LDH-0.22 | 0.22 | 1.5 ± 0.5 | 0.5 | 9.3 | >99 | 46500 | Ref. 23 |
| 15 | $Fe_3O_4$@$Ni_3$Al-LDH | - | - | 8 | 5.7 | >99 | - | This work |
| 16 | $Fe_3O_4$ | - | - | 8 | 1.1 | >99 | - | This work |

[a] Reaction conditions: 1 mmol 1-phenylethanol, Au catalyst (0.2 mol%), 5 mL toluene, 80 °C, 20 mL $min^{-1}$ $O_2$ (atm). [b] Moles of alcohol converted per mole of Au per hour. [c] 1 mmol 1-phenylethanol, Au catalyst (0.1 mol%), 5 mL toluene, 80 °C, 20 mL $min^{-1}$ $O_2$. [d] 5 mmol 1-phenylethanol, Au catalyst (0.01 mol%), 5 mL toluene, 80 °C, 20 mL $min^{-1}$ $O_2$. [e] 10 mmol 1-phenylethanol, Au catalyst (0.015 mol%), 10 mL toluene, 80 °C, 20 mL $min^{-1}$ $O_2$. [f] 1-phenylethanol (100 mmol), catalyst (Au: 4.0 × $10^{-4}$ mol%), $O_2$ (20 mL/min), 160 °C, 30 min. [g] 1 mmol 1-phenylethanol, Au catalyst (0.1 mol%), 5 mL toluene, 80 °C, pre-evacuation by Ar for 1 h before reaction, all in Ar (8 mL $min^{-1}$).

result is much better than those of the previously reported Au/$Zn_5(CO_3)_2(OH)_6$ (25000 $h^{-1}$)[43], Au/HT (37000 $h^{-1}$)[18], AuNCs/$Ni_3$Al-LDH (46500 $h^{-1}$)[23] (Table 1, entry 14) and comparable to $Au_{25}$/$Ni_3$Al-LDH (11840 $h^{-1}$)[24] (Table 1, entry 12) under the similar catalytic reaction conditions, clearly confirming the excellent aerobic oxidation activity for alcohols of the present hierarchical hollow core@shell magnetic catalysts.

In addition, γ-$Fe_2O_3$@$Ni_3$Al-LDH@$Au_{25}$-0.053 can also oxidize selectively a wide range of alcohols to corresponding carbonyl compounds with high activity, implying a high versatility of the nearly atomic precise gold catalyst. The γ-$Fe_2O_3$@$Ni_3$Al-LDH@$Au_{25}$-0.053 presents comparable or higher activities not only for benzylic secondary alcohols containing 1-phenylethanol and benzhydrol (Table 2, entries 1 and 5), but also for aliphatic secondary alcohols such as cyclohexanol (Table 2, entry 9), compared with previously reported Au/HT catalysts (Table 2, entries 2-4, 6-8 and 10-12) at high conversion.[18,23,44] Moreover, the γ-$Fe_2O_3$@$Ni_3$Al-LDH@$Au_{25}$-0.053 displays higher selective oxidation activity for benzylic primary alcohols (Table 2, entry 13), compared with literature values (Table 2, entries 14 and 15).[23,44] We also note that γ-$Fe_2O_3$@$Ni_3$Al-LDH@$Au_{25}$-0.053 shows high oxidation activity for allylic alcohols, for instance, cinnamyl alcohol can be selectively oxidized to cinnamyl aldehyde with 94.8% conversion in 4 h (Table 2, entry 16). All these results indicate that the present magnetic catalysts are highly effective for aerobic oxidation of alcohols.

Furthermore, the magnetic recyclability of γ-$Fe_2O_3$@$Ni_3$Al-LDH@$Au_{25}$-0.053 was explored. Typically, after reaction with 1-phenylalcohol, the catalyst was separated from the reaction mixture by an external magnetic field (0.15 T), thoroughly washed with toluene, then reused under identical conditions and the results show 99% conversion and 99% selectively in aerobic oxidation of 1-phenylethanol even in the 10th run (Table 2, entry 19). The HRTEM of the recovered catalyst (Fig. S8b) shows a similar $Au_{25}$NCs size (1.4 ± 0.5 nm) to the fresh one. Moreover, after the catalyst was separated from the reaction system, continued stirring of the filtrate under the same conditions did not give any products, and the ICP analysis of the filtrate indicates no Au present. These results confirm that the oxidation occurred on the $Au_{25}$NCs loaded on the surface of magnetic $Ni_3$Al-LDH and there is no loss and aggregation of $Au_{25}$NCs from the catalyst during the reaction. These findings clearly suggest the excellent structure stability and recycling efficiency of the present hierarchical hollow core@shell magnetic nano-gold catalyst.

**Table 2** Aerobic oxidation of various alcohols to corresponding carbonyl compounds over γ-$Fe_2O_3$@$Ni_3Al$-LDH@$Au_{25}$-0.053.[a]

| Entry | Substrate | Au loading / mol% | Conv. / % | Sel. / % | t / h |
|---|---|---|---|---|---|
| 1 | 1-phenylethanol | 0.115 | 99 | 99 | 0.5 |
| 2[b] | 1-phenylethanol | 0.115 | 99 | 99 | 0.5 |
| 3[c] | 1-phenylethanol | 0.45 | 99 | 99 | 0.33 |
| 4[d] | 1-phenylethanol | 0.25 | 99 | 99 | 4 |
| 5 | Benzhydrol | 0.115 | 99 | 99 | 3 |
| 6[b] | Benzhydrol | 0.115 | 99.9 | 99 | 4 |
| 7[c] | Benzhydrol | 0.45 | 99 | 96 | 4 |
| 8[d] | Benzhydrol | 0.25 | 99 | 99 | 4 |
| 9 | Cyclohexanol | 0.115 | 98.7 | 99 | 4 |
| 10[b] | Cyclohexanol | 0.115 | 98.3 | 99 | 4 |
| 11[c] | Cyclohexanol | 0.45 | 93 | 97.8 | 4 |
| 12[d] | Cyclohexanol | 0.25 | 11 | 99 | 4 |
| 13 | Benzylalcohol | 0.115 | 99 | 99 | 1.5 |
| 14[b] | Benzylalcohol | 0.115 | 95.3 | 99 | 2 |
| 15[d] | Benzylalcohol | 0.25 | 57 | 99 | 2 |
| 16 | Cinnamylalcohol | 0.115 | 94.8 | 93 | 4 |
| 17[b] | Cinnamylalcohol | 0.115 | 77 | 96 | 4 |
| 18[d] | Cinnamylalcohol | 0.45 | 54 | 99 | 2 |
| 19[e] | 1-phenylethanol | 0.115 | 99 | 99 | 0.5 |

[a] Reaction conditions: Alcohol (1 mmol), γ-$Fe_2O_3$@$Ni_3Al$-LDH@$Au_{25}$-0.053 (Au: 0.115%), toluene (5 mL), 80 °C, $O_2$ (atm) (20 mL min$^{-1}$ ). [b] Alcohol (1 mmol), AuNCs/$Mg_3Al$-LDH-0.23(Au:0.115%), toluene (5 mL), 80 °C, $O_2$ (atm) (20 mL min$^{-1}$) in ref 23. [c] Alcohol (1 mmol), Au/HT (0.1 g), toluene (5 mL), 80 °C, air (1 atm) in ref 18. [d] Alcohols (1 mmol), Au/2Ni-Al (0.05 g, Au 1wt%), toluene (20 mL), alcohol/Au=400 (mole ratio), 80 °C, $O_2$ (atm) (15 mL/min) in ref 44. [e] Oxidation results for the 10th run.

**The kinetics analysis of the catalysts.**

To reveal the nature reason for varied alcohol oxidation performance of the series γ-$Fe_2O_3$@$M_3Al$-LDH@$Au_{25}$-*x* catalysts, we study the macroscopic kinetic process of the present magnetic catalysts involving the effect of the varied supports and reaction temperatures on the reaction rate for the aerobic oxidation of 1-phenylethanol. Time-evolution of conversion, C, was monitored from the yield of product as shown in Fig. S9. It can be seen that the time-conversion plots are linear up to *ca.* 60% conversion of 1-phenylethanol in toluene (Fig. S9(a,b) except less active CuMg-based catalyst, implying that the product inhibition is very small. As shown in Fig. 6, the term -ln(1-C) is increased linearly with the reaction time (h) for all the γ-$Fe_2O_3$@$M_3Al$-LDH@$Au_{25}$-*x* catalysts, indicating that the reaction is first order with respect to 1-phenylethanol. The rate constant, *k*, was therefore obtained from the slope of the -ln(1-*C*) plot as a function of reaction time. The rate constant *k* for 1-phenylethanol oxidation at 60 – 100 °C in toluene was listed in Table S3. The *k* values of 1-phenylethanol oxidation with solvent at the same temperature are increased in an order of γ-$Fe_2O_3$@$Ni_3Al$-LDH@$Au_{25}$-0.23 > γ-$Fe_2O_3$@$Mg_3Al$-LDH@$Au_{25}$-0.21 > γ-$Fe_2O_3$@$Cu_{0.5}Mg_{2.5}Al$-LDH@$Au_{25}$-0.2.

A good linear correlation is obtained by plotting of ln*k* vs. the inverse of the temperature, and the apparent activation energy, $E_a$, could be estimated with the slope (Fig. 6, Table S3). The least-square fit analysis gives $E_a$ value as 19.2 kJ/mol for the optimal catalyst γ-$Fe_2O_3$@$Ni_3Al$-LDH@$Au_{25}$-0.23, which is smaller than γ-$Fe_2O_3$@$Mg_3Al$-LDH@$Au_{25}$-0.21 (23.4 kJ/mol) and γ-$Fe_2O_3$@$Cu_{0.5}Mg_{2.5}Al$-LDH@$Au_{25}$-0.2 (26.7 kJ/mol) in toluene. The highest *k* and the lowest $E_a$ of γ-$Fe_2O_3$@$Ni_3Al$-LDH@$Au_{25}$-0.23 imply its optimal electron structure of ultrafine and nearly atomic precise $Au_{25}$NCs and enhanced $Au_{25}$NCs – $Ni_3Al$-OH intercation associated with the ultrafine $Au_{25}$NCs and honeycomb-like ultrathin $Ni_3Al$-LDH naoplates.

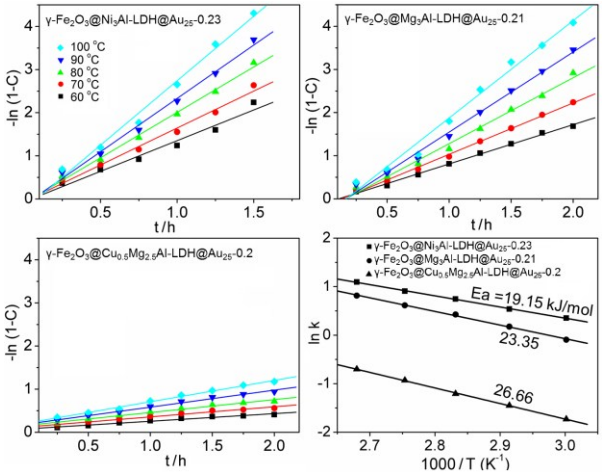


**Fig. 6** –ln(1-C) against time (a-c) and Arrhenius plots (d) for the aerobic oxidation of 1-phenylethanol on γ-$Fe_2O_3$@$M_3Al$-LDH@$Au_{25}$-*x* (*x*~0.2) at temperatures of 60, 70, 80, 90 and 100 °C. Reaction conditions: 1-phenylethanol (1 mmol), catalyst (Au: 0.2 mol%), toluene (5 mL), $O_2$ (20 mL/min).

Based on previous XRD (Fig. 2), Raman (Fig. S4) and clear color change from black to brick-red (photo in Fig. 1), the phase transformation from $Fe_3O_4$ to γ-$Fe_2O_3$ occurred in the catalysts on calcinations, while the pure $Fe_3O_4$@$M_3Al$-LDH supports failed to show these conversion with similar treatment, implying the facilitation of $Au_{25}Capt_{18}$ on the phase translation of magnetite core. Therefore, it can be expected that three-phase synergistic effect probably occurs among the $Au_{25}$NCs, the LDH shell and the magnetic core besides the commonly reported gold – LDH interactions in LDH supported gold catalysts[23,24,44]. Thus, the unprecedentedly high aerobic oxidation activity of the present magnetic catalysts especially the γ-$Fe_2O_3$@$Ni_3Al$-LDH@$Au_{25}$-0.053 for 1-phenylethanol can be ascribed not only to the nearly atomic precise monodispersion of $Au_{25}$NCs and regular $Ni_3Al$-LDH with ultrathin nanoplates, but also to the strongest $Au_{25}$NCs – Ni-OH interaction and $Au_{25}$NCs – LDH – magnetic core three-phase synergetic effect. Firstly, the deposition of nearly atomic precise $Au_{25}$NCs may provide more favorable surface electronic state of $Au_{25}$ thus develop a highly active $Au_{25}$NCs catalyst probably through a beneficial modification for electronic structure of the Au core. Then, the electron transfer from the magnetic core to $Ni_3Al$-LDH shell occurred and followed the continued electron transfer from the $Ni_3Al$-LDH shell to the $Au_{25}$NCs resulting in increased electron cloud density surrounding $Au_{25}$NCs. Clearly, the intermediate LDH shell, especially the $Ni_3Al$-OH groups may significantly improve the monodispersion of $Au_{25}$NCs onto the edges sites of ultrathin LDH nanoplates thus effectively strengthen the $Au_{25}$NCs – LDH synergetic interaction, compared to the pure LDH supported mixed Au clusters catalysts.[23]

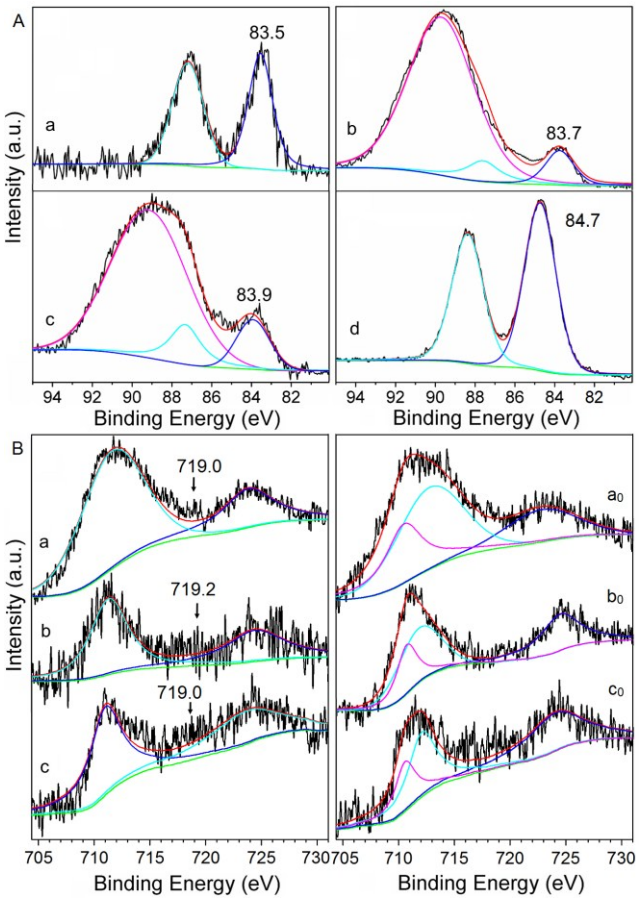


**Fig. 7** Au 4f (A) and Fe 2p (B) XPS spectra of γ-$Fe_2O_3$@$Ni_3$Al-LDH@$Au_{25}$-0.23 (a), γ-$Fe_2O_3$@$Mg_3$Al-LDH@$Au_{25}$-0.21 (b), γ-$Fe_2O_3$@$Cu_{0.5}Mg_{2.5}$Al-LDH@$Au_{25}$-0.2 (c) compared with $Au_{25}Capt_{18}$ (d) and corresponding supports ($a_0$-$c_0$).

**The XPS analysis of the catalysts.**

The XPS analysis (Fig. 7) was employed to further explore the correlation between the catalytic activity and the electron structure of the magnetic catalysts. The XPS spectra of $Au_{25}Capt_{18}$ (Fig. 7A(d)) show the Au $4f_{7/2}$ binding energy (BE) at 84.7 eV, *ca*. 0.7 eV higher than 84.0 eV of bulk gold, which can be attributed to partial charge transfer from Au to S,[21,45] approving the formation of Au-S bond for $Au_{25}Capt_{18}$. While for the catalysts γ-$Fe_2O_3$@$Ni_3$Al-LDH@$Au_{25}$-0.23 (Fig. 7A(a)), γ-$Fe_2O_3$@$Mg_3$Al-LDH@$Au_{25}$-0.21 (Fig. 7A(b)), and γ-$Fe_2O_3$@$Cu_{0.5}Mg_{2.5}$Al-LDH@$Au_{25}$-0.2 (Fig. 7A(c)), the Au $4f_{7/2}$ BE values of 83.5, 83.7 and 83.9 eV, respectively, are clearly smaller than that of bulk Au, assigned to the lower coordination number of surface Au atoms of ultrasmall $Au_{25}$NCs,[46] indicating the negatively charged nature of $Au_{25}$NCs on the catalysts[41,47,48] and an electron transfer from shell LDH to the surface of $Au_{25}$NCs[21,49]. Given that the electron affinity of neutral gold nanoparticle is size-dependent,[50] as the Au size is remarkably reduced to below 5 nm, surface Au atoms on the nanoparticles behave more like a single Au atom, are highly active and easily anionically ionized. The electron affinity of a single Au atom is 2.3 eV,[50] which is larger than the threshold value of electron transfer. The driving force for electron transfer from the LDH surface to Au atoms originates from surface conjugation and the differential Fermi energy level. It takes some charge to equalize the Fermi levels.[50,51] The Au $4f_{7/2}$ BE values of γ-$Fe_2O_3$@$Ni_3$Al-LDH@$Au_{25}$-0.23, γ-$Fe_2O_3$@$Mg_3$Al-LDH@$Au_{25}$-0.21, and γ-$Fe_2O_3$@$Cu_{0.5}Mg_3$Al-LDH@$Au_{25}$-0.2 show 0.5, 0.3 and 0.1 eV downshift from the bulk Au, respectively, indicating that the number of electrons transferred from shell LDH to $Au_{25}$NCs increases sequentially as γ-$Fe_2O_3$@$Cu_{0.5}Mg_{2.5}$Al-LDH@$Au_{25}$-0.2 < γ-$Fe_2O_3$@$Mg_3$Al-LDH@$Au_{25}$-0.21 < γ-$Fe_2O_3$@$Ni_3$Al-LDH@$Au_{25}$-0.23. This trend is in good agreement with the activity results, just as Tsukuda *et al*.[47] reported that the catalytic activity of Au NPs for aerobic oxidations is enhanced by an increase in the amount of negative charge on the Au core, therefore further suggesting that the interaction between the $Au_{25}$NCs and the different shell LDH of the magnetic catalysts.

In order to get more insight into the nature of the present hierarchical hollow core@shell magnetic nano-gold catalysts, Fe 2p (Fig. 7B), M(II) 2p (Fig. S10) and O 1s (Fig. S11) spectra were carefully analysed for the catalysts compared with corresponding supports and the parameters summarized in Table S4. The Fe 2p XPS spectra of the $Fe_3O_4$@$M_3$Al-LDH supports (Fig. 7$a_0$-$c_0$) show two distinct broad peaks for Fe $2p_{3/2}$ and Fe $2p_{1/2}$, and the deconvolution BE of Fe $2p_{3/2}$ are 710.5 and 712.8 eV, 710.7 and 711.8 eV, and 710.6 and 712.1 eV for Ni-, Mg-, and CuMg-based supports, respectively, which can be assigned to the $Fe^{2+}$ and $Fe^{3+}$ cations in $Fe_3O_4$,[26] consistent with the above XRD and Raman data. However, the Fe 2p XPS spectra of γ-$Fe_2O_3$@$Ni_3$Al-LDH@$Au_{25}$-0.23, γ-$Fe_2O_3$@$Mg_3$Al-LDH@$Au_{25}$-0.21 and γ-$Fe_2O_3$@$Cu_{0.5}Mg_{2.5}$Al-LDH@$Au_{25}$-0.2 (Fig. 7e-g) show the relatively narrow Fe $2p_{3/2}$ peak at 711.9, 711.3, and 711.4 eV accompanied by a satellite at ~719.1 eV (marked by an arrow), respectively, assigned to the $Fe^{3+}$ species, suggesting the presence of γ-$Fe_2O_3$ phase in the catalysts.[52] Noted that these Fe $2p_{3/2}$ peaks show *ca*. 1.2, 0.6 and 0.7 eV higher than that of γ-$Fe_2O_3$ at 710.7 eV[53], which can be attributed to partial charge transfer from iron oxide core to the LDH shell.

Simultaneously, the main peak of Ni $2p_{3/2}$ at 856.8 eV (Fig. S10) of γ-$Fe_2O_3$@$Ni_3$Al-LDH@$Au_{25}$-0.23 clearly upshifts compared with the support, implying the decrease in electron density around Ni core level. These results clearly suggest the electron transfer from iron oxide core to the $Ni_3$Al-LDH shell and then to the $Au_{25}$NCs, in line with above obvious Au $4f_{7/2}$ downshift, suggesting the possible $Au_{25}$NCs – LDH – magnetic core three-phase juncture linkage. Then for γ-$Fe_2O_3$@$Mg_3$Al-LDH@$Au_{25}$-0.21, the peak at 50.1 eV assigned to Mg $2p_{3/2}$ core level shows close BE value and intensity to $Fe_3O_4$@$Mg_3$Al-LDH, implying the relatively weak $Au_{25}$NCs – LDH – magnetic core three-phase interaction, consistent with the small Au 4f downshift. As for γ-$Fe_2O_3$@$Cu_{0.5}Mg_{2.5}$Al-LDH@$Au_{25}$-0.2, Cu $2p_{3/2}$ shows small but detectable upshift compared with the $Fe_3O_4$@$Cu_{0.5}Mg_{2.5}$Al-LDH, implying the relatively less electron transfer from magnetic core to the shell CuMgAl-LDH and then to the $Au_{25}$NCs upon the lower Cu content, in line with the observed Au 4f downshift.

The curve fittings of O 1s spectra (Fig. S11) of the magnetic catalysts and corresponding supports reveal that there are two oxygen species including surface OH and lattice $O^{2-}$ species. The curve fitting of O 1s spectrum of γ-$Fe_2O_3$@$Ni_3$Al-LDH@$Au_{25}$-0.23 reveals that surface OH species (45.1%) is 2.5% lower than

those of $Fe_3O_4$@$Ni_3$Al-LDH (47.6%) and the surface OH species of γ-$Fe_2O_3$@ $Mg_3$Al-LDH@$Au_{25}$-0.21 (42.1%) is 4.1% lower than that of $Fe_3O_4$@$Mg_3$Al-LDH (46.2%), while for γ-$Fe_2O_3$@$Cu_{0.5}Mg_{2.5}$Al-LDH@$Au_{25}$-0.2, the surface OH species (41.3%) is 3.4% lower than that of $Fe_3O_4$@$Cu_{0.5}Mg_{2.5}$Al-LDH (44.7%). Dai *et al.*[48] studied the interaction between gold nanoclusters and a fully hydroxylated surface, $Mg(OH)_2$'s basal plane using DFT theory and found strong interaction of Au clusters with the surface –OH *via* a short bond between edge Au atoms and O atoms of the –OH groups helping the Au clusters against sintering and stabilizing Au clusters *via* Au-OH linkage and thereby affording to their CO-oxidation activity. Combining the catalytic results with systematic characterization analyses, the electron-rich $Au_{25}$NCs in the present magnetic catalysts is more likely to be originated from the existence of large amount of hydroxyl functional groups on the supports as O 1s spectra revealed (Fig. S11), though the magnetic catalysts hold varied amount of hydroxyl groups upon varied kinds of metal cations on magnetic LDH supports.

**The CO adsorption FT-IR analysis of the catalysts.**

The electronic state of $Au_{25}$NCs and the surface acidity of the γ-$Fe_2O_3$@$M_3$Al-LDH@$Au_{25}$-*x* catalysts were further tentatively studied by using CO adsorption along with FT-IR technique and shown in Fig. 8. In order to discriminate between the adsorption properties of the surface Au atoms and the magnetic supports, CO adsorption was first studied on pristine magnetic supports. Three $Fe_3O_4$@$M_3$Al-LDH supports did not show any pronounced IR bands in the region 2000–2130 $cm^{-1}$ when exposed to a CO flow. Only prominent broad bands located at *ca.* 2171 $cm^{-1}$ were found. These bands can be assigned to the stretching mode of CO adsorbed on Brønsted acid sites related to AlO-$H^{\delta+}$ centres.[17,54,55] Wang *et al.*[17] and Corma's group[55] have ever revealed the strong acidity and basicity of the LDH and LDH-derived materials. It is believed that CO molecules could be atop bound to Au atoms of nanoclusters and surfaces, thus, the stretching mode $\nu_{CO}$ of adsorbed CO mainly reflects the electron density on the adsorption sites, and the $\nu_{CO}$ is red- and blue-shifted compared with that of free CO as CO is adsorbed on anionic and cationic Au sites, respectively.[56-59] In the present work, it can be clearly

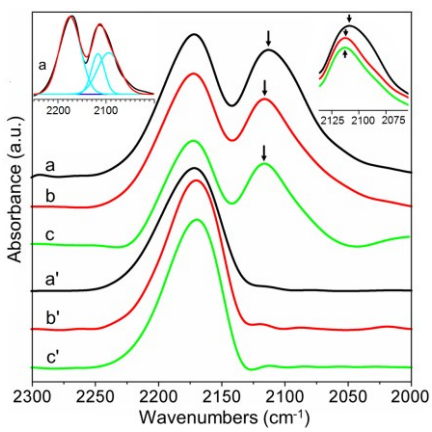


**Fig. 8** CO adsorption FTIR spectra of γ-$Fe_2O_3$@$Ni_3$Al-LDH@$Au_{25}$-0.23 (a), γ-$Fe_2O_3$@$Mg_3$Al-LDH@$Au_{25}$-0.21 (b) and γ-$Fe_2O_3$@$Cu_{0.5}Mg_{2.5}$Al-LDH@$Au_{25}$-0.2 (c) compared with corresponding $Fe_3O_4$@LDH supports (a', b', c').

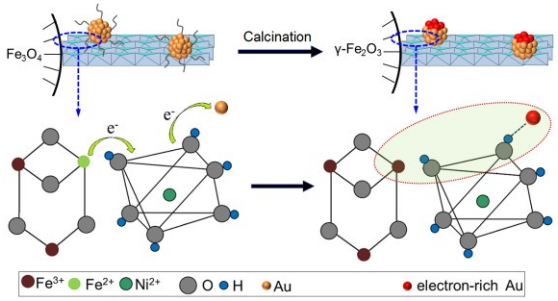


**Scheme 2.** The nature of active sites of γ-$Fe_2O_3$@$M_3$Al-LDH@$Au_{25}$-*x* catalysts.

seen that besides the features at ~2171 $cm^{-1}$ due to the CO adsorbed on the supports, prominent IR bands indicated by arrows at 2106, 2110 and 2112 $cm^{-1}$ for γ-$Fe_2O_3$@$Ni_3$Al-LDH@$Au_{25}$-0.23, γ-$Fe_2O_3$@$Mg_3$Al-LDH@$Au_{25}$-0.21 and γ-$Fe_2O_3$@$Cu_{0.5}Mg_{2.5}$Al-LDH@$Au_{25}$-0.2, respetively, display clear red-shift, compared to literature signals in the region of 2113 and 2125 $cm^{-1}$ assigned to $Au^0$ carbonyls of Au NPs.[49,60-62] These obvious red-shift of the CO band can be attributed to the greater π back-donation from the negatively charged $Au_{25}$ nanoclusters.

It is also carefully noticed that all the bands indicated by arrows assigned to CO adsorbed on $Au_{25}$NCs show an asymmetric broadening from the low-frequency side, which may be related to CO adsorbed on sites at the perimeter between $Au_{25}$NCs and supports of the catalysts considering their absence in single supports and the similarity to previous reports.[7,43,63] Especially for γ-$Fe_2O_3$@$Ni_3$Al-LDH@$Au_{25}$-0.23, the greatly broadening peak at 2106 $cm^{-1}$ can be decomposed into two bands at 2098 and 2112 $cm^{-1}$ (Fig. 8 inset (a)), which correspond to atop bound CO on the outer layer Au and to CO adsorbed on sublayer Au, respectively, according to the previously intensive studies on Au/$TiO_2$ catalysts by Goodman[56] and Boccuzzi[64]. These observed $\nu_{CO}$ frequencies demonstrate that the $Au_{25}$NCs on $Ni_3$Al-LDH-based support are electron-rich, for instance $Au^{\delta-}$, and that the extent of electron transfer from the support to the gold cluster is more than those on γ-$Fe_2O_3$@$Mg_3$Al-LDH@$Au_{25}$-0.21 and γ-$Fe_2O_3$@$Cu_{0.5}Mg_{2.5}$Al-LDH@$Au_{25}$-0.2. These results are consistent with the XPS analysis and alcohol oxidation activities, suggesting the more negatively charged $Au_{25}$NCs on the catalysts is more favourable for the oxidation of alcohols.

Based on above results and discussions, it appears that the larger electronegativities of transition metals nickel than magnesium and copper on the LDH layers may easily facilitate the electron transfer from the LDH support to gold nanoclusters and probably results in more electron-rich gold cores on γ-$Fe_2O_3$@$Ni_3$Al-LDH@$Au_{25}$-0.23 than on γ-$Fe_2O_3$@$Cu_{0.5}Mg_{2.5}$Al-LDH@$Au_{25}$-0.2 and γ-$Fe_2O_3$@$Mg_3$Al-LDH@$Au_{25}$-0.21. In fact, the downshifts of the Au $4f_{7/2}$ peak and the red-shifts of CO adsorption of the catalysts are observed with a decreasing order of γ-$Fe_2O_3$@$Ni_3$Al-LDH@$Au_{25}$-0.23 > γ-$Fe_2O_3$@$Mg_3$Al-LDH@$Au_{25}$-0.21 > γ-$Fe_2O_3$@$Cu_{0.5}Mg_{2.5}$Al-LDH@$Au_{25}$-0.2, which is attributable to the larger amount of electronic charge deposited on the Au cores of the $Au_{25}$NCs supported on magnetic LDH supports containing large amount of transition metal cations. These analysis results are in good agreement with the alcohol oxidation activities of these catalysts enhanced with an increased order of γ-$Fe_2O_3$@$Cu_{0.5}Mg_{2.5}$Al-LDH@$Au_{25}$-0.2 < γ-

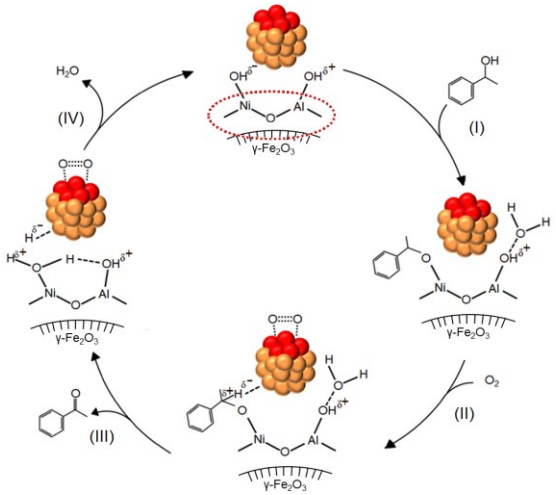


**Scheme 3** Mechanism of areobic oxidation for alcohol of the magnetic $Au_{25}$NCs catalysts using γ-$Fe_2O_3$@$Ni_3$Al-LDH@$Au_{25}$-*x* as example.

$Fe_2O_3$@$Mg_3$Al-LDH@$Au_{25}$-0.21 < γ-$Fe_2O_3$@$Ni_3$Al-LDH@$Au_{25}$-0.23 (Table 1).

The present results imply that the strong $Au_{25}$NCs – LDH interactions together with the possible $Au_{25}$NCs – LDH–magnetic core three-phase synergy featured as effect on the electronic structure of the $Au_{25}$NCs play key roles on the various aerobic alcohol oxidation activity of the γ-$Fe_2O_3$@$M_3$Al-LDH@$Au_{25}$-*x* catalysts. Meanwhile, unprecedentedly higher oxidation activity of γ-$Fe_2O_3$@$Ni_3$Al-LDH@$Au_{25}$-0.053 than most previously reported catalysts may also be benefited from the existence of Brønsted basic sites (M-$OH^{\delta-}$) on the catalysts for the initial O-H bond cleavage, as most reports pointed previously,[17,18,23,24,43] as well as the existence of surface nickel sites and the nearly atomic precise $Au_{25}$NCs for improving the cleavage of C-H band to create the carbonyl compound. The existence of Brønsted acid sites on the surface of the catalysts may also facilitate the alcohol oxidation process as Wang *et al*. reported.[17] Based on the above analysis, the nature of the active sites of the γ-$Fe_2O_3$@$M_3$Al-LDH@$Au_{25}$-*x* catalysts are illustrated in Scheme 2.

The effect of electronic structures of gold clusters on aerobic alcohol oxidation has been previously studied by Tsukuda *et al*.[38,47], and the cleavage of the C-H bond at the benzylic position is accepted as the rate-determining step through kinetic isotope effect. Particularly, Tsukuda and co-workers[47] reported the catalytic property of colloidal Au nanoclusters with varying sizes (1.0-3.0 nm) stabilized by poly(N-vinyl-2-pyrrolidone) or poly (allylamine) for dehydrogenation of p-hydroxybenzyl alcohols in the presence of $O_2$ in water with $K_2CO_3$ additive, and found that the smaller Au clusters exhibited higher catalytic activity. Based on various spectroscopic studies, they further revealed that the higher activity of the smaller Au nanoclusters was due to the increased negative charge on the Au core surrounded by the organic stabilizer, and proposed that an extra electron from the Au readily transfers to the anti-bonding 2π* orbital of the $O_2$ adsorbed, based on similar observations of Au cluster anions *via* gas-phase studies,[61,65] thus weakens the O-O bond and activates $O_2$ molecules to form superoxo- or peroxo-like species for further catalytic reaction, which may play an crucial role in the alcohol oxidations. The present lower activation energy $E_a$ for aerobic alcohol oxidation over γ-$Fe_2O_3$@$Ni_3$Al-LDH@$Au_{25}$-0.23 also implies strongly the electron-rich $Au_{25}$NCs and the strongest $Au_{25}$NCs – $Ni_3$Al-LDH interaction assisted by $Au_{25}$NCs – shell $Ni_3$Al-LDH – magnetic core three-phase synergetic effect, in line with its greatly enhanced catalytic activity.

The generally accepted view for the aerobic oxidation of alcohols catalysed by LDH-supported Au catalysts contains the assumption that the rate-determining step, the *β*-H elimination of a metal alkoxide intermediate on the heterogeneous metal surface, is the same on metal oxides loaded noble metal catalysts,[6,66] and specially, the intrinsic basic sites on the LDH-based supports activate the O-H bond of the alcohols to promote the formation of the metal alkoxide intermediate.[2,18,42,43] The activation of oxygen by supported metals[67] or surface oxygen vacancies of the supports[5] is another critical step for generation of water.

On the basis of all the above experimental and characteristic results and the previous findings,[2,18,24,44,67] we tentatively propose a possible aerobic oxidation mechanism of alcohols on magnetic catalysts γ-$Fe_2O_3$@$M_3$Al-LDH@$Au_{25}$-*x* (Scheme 3). In step (I), hydroxyl hydrogen of alcohol molecule attacks a weak basic Ni-$OH^{\delta-}$ site on the shell $Ni_3$Al-LDH, resulted from an abstraction of proton by the hydroxyl groups on the support, to promote the formation of Ni-alkoxide intermediate at the interface and the simultaneous generation of a water molecule. In step (II), $O_2$ molecules adsorbed on the Au sites near the interface between $Au_{25}$NCs and the LDH shell is directly activated *via* the double linear $O_s$-Au-$O_a$ model,[68] and the hydrogen atom on the *β*-carbon of the intermediate [Ni-alkoxide]$^-$ is simultaneously coordinated with $Au_{25}$NCs. This adsorption-desorption equilibrium could be achieved rapidly in Step (I) or (II) upon the promotion of electron transfer to $O_2$.[66] In step (III), also considered as the rate-determining step,[6,7,66] the [Ni-alkoxide]$^-$ intermediate undergoes a *β*-H elimination assisted by the radical-like peroxo-species to afford metal-hydride species (Au-$H^{\delta-}$) at the interface of the catalysts[69] along with the formation of corresponding carbonyl product. The coordinatively unsaturated metal atoms are more active for the cleavage of this C–H bond with the assistance of Au-O-O-Au species. Therefore, the present hierarchical hollow nanostructured magnetic catalysts with nearly atomic precise $Au_{25}$NCs exhibit much higher catalytic activity. Final step (IV), the Au-$H^{\delta-}$ hydride is oxidized quickly by adsorbed active oxygen to form a water molecule with the adsorbed $H^{\delta+}$, which is promoted by the AlO-$H^{\delta+}$ acidic sites on the catalyst surface.[17,24] Thus, the original metallic sites are recovered to complete the catalytic oxidation cycle. Based on this reaction mechanism, the present 3D honeycomb-like hierarchical nanostructured LDH-based magnetic support especially $Fe_3O_4$@$Ni_3$Al-LDH with small ultrathin nanoplates providing uniform distribution of $Ni_3$Al-OH groups, which is the key factor for the *β*-H elimination of metal alkoxide by the strongest synergetic effect between the nearly atomic precise $Au_{25}$NCs and the core@shell magnetic LDH support, besides the promotion effect of the weak Brønsted base sites on the LDH supports. Moreover, the good magnetization property of the hierarchical hollow nanostructured $Au_{25}$NCs catalysts greatly faciliatates their recycling efficiency in the alcohol oxidation reaction and these magnetic catalysts are highly desired to apply in a large variety of heterogeneous catalysis processes.

## Conclusions

In summary, we have successfully assembled a series of 3D honeycomb-like hierarchical hollow nanostructured magnetic catalysts γ-$Fe_2O_3$@$M_3$Al-LDH@$Au_{25}$-*x* (*x* refers to the measured mass of Au in wt%) by a modified electrostatic adsorption method using water-soluble captopril-capped $Au_{25}$ nanoclusters ($Au_{25}Capt_{18}$) as precursor followed by proper calcinations. The synergetic interaction between $Au_{25}$ nanoclusters ($Au_{25}$NCs) and magnetic LDH-based support along with sintering effect results in slightly aggregated $Au_{25}$NCs for the series γ-$Fe_2O_3$@$M_3$Al-LDH@$Au_{25}$-*x* (*x*~0.2) catalysts (ca. 3.0 ± 1.3，3.3 ± 1.2 and 4.2 ± 1.5 nm for Ni-, Mg-, and CuMg-based catalysts, respectively) on calcinations. While the lower gold loading catalysts γ-$Fe_2O_3$@$Ni_3$Al-LDH@$Au_{25}$-*x* (*x* =0.053, 0.11) show nearly atomic precise $Au_{25}$NCs (*ca*. 1.4 ± 0.3 – 1.9 ± 0.6 nm) highly dispersed on the surface of shell $Ni_3$Al-LDH. All the γ-$Fe_2O_3$@$M_3$Al-LDH@$Au_{25}$-*x* catalysts exhibit much higher catalytic activity than $Fe_3O_4$@$Mg_3$Al-LDH@Au by conventinal DP method for the oxidation of 1-phenylethanol in toluene under atmospheric oxygen without basic additive. Particularly, the γ-$Fe_2O_3$@$Ni_3$Al-LDH@$Au_{25}$-0.053 exhibits the highest activity (TOF: 112498 $h^{-1}$) for the aerobic oxidation of 1-phenylethanol under solvent-free conditions and can be applied for a wide range of alcohols, which can be mainly ascribed to the nearly atomic precise electron-rich $Au_{25}$NCs and remarkable $Au_{25}$NCs – $Ni_3$Al-LDH – magnetic core three-phase synergetic effect along assisted by abundant Ni-OH sites. Moreover, the catalyst γ-$Fe_2O_3$@$Ni_3$Al-LDH@$Au_{25}$-0.053 was simply separated by using an external magnetic field and recycled more than ten times without any significant loss of activity, rendering the magnetic catalyst long-term stability. The present study offers a novel strategy for fabricating environmentally benign hollow nanostructured $Fe_3O_4$@LDH supported gold nanoclusters catalysts for highly efficient aerobic oxidation of alcohols, and also allows the metal nanocluster precursor method to be used in other noble or nonprecious metal-supported recyclable catalysts with easily controlled ultrafine metal clusters for a wide range of potential heterogeneous catalysis applications.

## Acknowledgements

This work was supported by National Natural Science Foundation of China (21276015, 21576013) and the Fundamental Research Funds for the Central Universities (YS1406).

## Notes and references

*State Key Laboratory of Chemical Resource Engineering, Beijing University of Chemical Technology, P.O. Box 98, Beijing 100029, China. Email: huizhang67@gst21.com; Fax: +8610-6442 5385; Tel.: +8610-6442 5872*

† Electronic Supplementary Information (ESI) available: [details of any supplementary information available should be included here]. See DOI: 10.1039/b000000x/

1 D. I. Enache, J. K. Edwards, P. Landon, B. Solsona-Espriu, A. F. Carley, A. A. Herzing, M. Watanabe, C. J. Kiely, D. W. Knight, G. J. Hutchings, *Science*., 2006, **311**, 362-365.
2 C. Parmeggiani and F. Cardona, *Green Chem.*, 2012, **14**, 547-564.
3 A. Corma, S. Iborra and A. Velty, *Chem. Rev.*, 2007, **107**, 2411-2502.
4 T. Wang, H. Shou, Y. Kou and H. Liu, *Green Chem.*, 2009, **11**, 562-568.
5 T. Mitsudome, Y. Mikami, H. Funai, T. Mizugaki, K. Jitsukawa and K. Kaneda, *Angew. Chem., Int. Ed.*, 2008, **47**, 138-141.
6 A. Abad, P. Concepción, A. Corma and H. García, *Angew. Chem. Int. Ed.*, 2005, **44**, 4066-40694.
7 A. Villa, C. E. Chan-Thaw, G. M. Veith, K. L. More, D. Ferri and L. Prati, *ChemCatChem.*, 2011, **3**, 1612–1618.
8 S. Shylesh, V. Schünemann and W. R. Thiel, *Angew. Chem. Int. Ed.*, 2010, **49**, 3428-3459.
9 T. Y. Cheng, D. C. Zhang, H. X. Li and G. H. Liu, *Green Chemistry.*, 2014, **16**, 3401-3427.
10 J. M. Zheng, Y. L. Dong, W. F. Wang, Y. H. Ma, J. Hu, X. J. Chen and X. G. Chen, *Nanoscale*, 2013, **5**, 4894–4901.
11 L, Zhou, C. Gao and W.J. Xu, *Langmuir.*, 2010, **26**, 11217–11225.
12 F. Mi, X. T. Chen, Y. W. Ma, S. T. Yin, F. L. Yuan and H. Zhang, *ChemCommun*., 2011, **47**, 12804-12806.
13 H. Zhang, G. Y. Zhang, X. Bi and X. T. Chen, *J. Mater. Chem.* A., 2013, **1**, 5934–5942.
14 W. Wu, C. Z. Jiang and V. A. L. Roy, *Nanoscale*, 2015, **7**, 38-58.
15 Z. Wu, S. Yang and W. Wu, *Nanoscale*, 2016, **8**, 1273-1259.
16 M. Valden, X. Lai and D. W. Goodman, *Science*, 1998, **281**, 1647-1650.
17 W. H. Fang, J. S. Chen, Q. H. Zhang, W. P. Deng and Y. Wang, *Chem. Eur. J.*, 2011, **17**, 1247-1256.
18 T. Mitsudome, A. Noujima, T. Mizugaki, K. Jitsukawa and K. Kaneda, *Adv. Synth. Catal.*, 2009, **351**, 1890-1896.
19 M. Brust, M. Walker, D. Bethell, D. J. Schiffrin and R. Whyman, *J. Chem. Soc., Chem. Commun*., 1994, 801-802.
20 A. C. Templeton, W. P. Wuelfing and R. W. Murray, *Acc. Chem. Res.*, 2000, **33**, 27-36.
21 Y. Negishi, K. Nobusada and T. Tsukuda, *J. Am. Chem. Soc.*, 2005, **127**, 5261-5270.
22 R. C. Jin, *Nanoscale.*, 2010, **2**, 343-362.
23 L. Li, L. G. Dou and H. Zhang, *Nanoscale.*, 2014, **6**, 3753-3763.
24 S. Wang, S. Yin, L. Li and H. Zhang, *Catal. Sci. Technol.* 2016, **6,** 4090-4104.
25 Q. Q. Xiong, J. P. Tu, Y. Lu, J. Chen, Y. X. Yu, Y. Q. Qiao, X. L. Wang and C. D. Gu, *J. Phys. Chem. C.*, 2012, **116**, 6495-6502.
26 T. Fan, D. K. Pan and H. Zhang, *Ind. Eng. Chem. Res.*, 2011, **50**, 9009-9018.
27 S. Kumar adn R. C. Jin, *Nanoscale*, 2012, **4**, 4222-4227.
28 H. Zhang, K. Zou, S. H. Guo and X. Duan, *J. Solid State Chem.*, 2006, **179**, 1792-1801.
29 M. Zhu, C. M. Aikens, F. J. Hollander, G. C. Schatz, R. C. Jin, *J. Am. Chem. Soc.*, 2008, **130**, 5883-5885.
30 M. Z. Zhu, W. T. Eckenhoff, T. Pintauer and R. C. Jin, *J. Phys. Chem. C.*, 2008, **112**, 14221-14224.
31 J. P. Ge, Y. X. Hu, M. Biasini, W. P. Beyermann and Y. D. Yin, *Angew. Chem., Int. Ed.*, 2007, **46**, 4342 −4345.
32 P. S. Braterman, Z. P. Xu, F. Yarberry, *in Handbook of Layered Materials*; ed. S. M. Auerbach, K. A. Carrado, P. K. Dutta, Marcel Dekker, New York, 2004, p. 373.
33 X. T. Chen, F. Mi, H. Zhang and H. Q. Zhang, *Mater. Lett.* 2012, **69**, 48-51.
34 X. Bi, T. Fan and H. Zhang, *ACS Appl. Mater. Interfaces*, 2014, **6**, 20498-20509.
35 W. Wu, Z. H. Wu, T. Yu, C. Z. Jiang and W. Kim, *Sci. Technol. Adv. Mater*., 2015, **16**, 023501.
36 D. L. A. de Faria, S. V. Silva and M. T. de Oliveira, *J. Raman Spectrosc.* 1997, **28**, 873-878.
37 J. A. Gursky, S. D. Blough, C. Luna, C. Gomez, A. N. Luevano and E. A. Gardner, *J. Am. Chem. Soc.*, 2006, **128**, 8376–8377.
38 Y. M. Liu, H. Tsunoyama, T. Akita, S. H. Xie and T. Tsukuda, *ACS Catal*., 2011, **1**, 2-6.
39 J. Liu, *ChemCatChem*., 2011, **3**, 934-948.
40 G. B. Sun, B. X. Dong, M. H. Cao, B. Q. Wei and C. W. Hu, *Chem. Mater.*, 2011, **23**, 1587-1593.
41 Y. M. Liu, H. Tsunoyama, T. Akita and T. Tsukuda, *Chem. Commun.*, 2010, **46**, 550-552.
42 L. Wang, J. Zhang, X. J. Meng, D. F. Zheng and F. S. Xiao, *Catal. Today.*, 2011, **175**, 404-410.

43 J. Yang, Y. J. Guan, T. Verhoeven, R. V. Santen, C. Li and E. J. M. Hensen, *Green Chem.*, 2009, **11**, 322– 325.
44 J. Wang, X. J. Lang, B. Zhaorigetu, M. L. Jia, J. Wang, X. F. Guo and J. C. Zhao, *ChemCatChem.*, 2014, **6**, 1737-1747.
45 X. T. Nie, C. J. Zeng, X. G. Ma, H. F. Qian, Q. J. Ge, H. Y. Xu and R. C. Jin, *Nanoscale.*, 2013, **5**, 5912-5918.
46 J. Radnik, C. Mohr and P. Claus, *Phys. Chem. Chem. Phys.*, 2003, **5**, 172-177.
47 H. Tsunoyama, N. Ichikuni, H. Sakurai and T. Tsukuda, *J. Am. Chem. Soc* , 2009, **131**, 7086-7093.
48 D. Jiang, S. H. Overbury and S. Dai, *J. Phys. Chem. Lett*., 2011, **2**, 1211–1215.
49 Y. Negishi, M. Mizuno, M. Hirayama, M. Omatoi, T. Takayama, A. Iwase and A. Kudo, *Nanoscale.*, 2013, **5**, 7188-7192.
50 J. A. Smith, M. Josowicz, M. Engelhard, D. R. Baer and J. Janata, *Phys. Chem. Chem. Phys.*, 2005, **7**, 3619-3625.
51 F. Wang, W. Ueda and J. Xu, *Angew. Chem. Int. Ed.*, 2012, **51**, 3883-3887.
52 Cornell, R.; Schwertmann, U.The Iron Oxides: Structure, Properties, Reactions, Occurrence and Uses; VCH, Weinheim, New York, 1996.
53 T. Fujii, F. M. F. de Groot, G. A. Sawatzky, F. C. Voogt, T. Hibma and K. Okada, Phys. Rev. B., 1999,59, 3195-3202.
54 G. B. Superti, E. C. Oliveira and H. O. Pastore, Chem. Mater., 2007, **19**, 4300–4315.
55 M. J. Climent, A. Corma, P. De Frutos, S. Iborra, M. Noy, A. Velty and P. Concepción, *J. Catal.*, 2010, **269**, 140-149.
56 M. S. Chen and D. W. Goodman, *Acc. Chem. Res.*, 2006, **39**, 739-746.
57 A. Fielicke, G. V. Helden, G. Meijer, B. Simard and D. M. Rayner, *J. Phys. Chem. B.*, 2005, **109**, 23935-23940.
58 H. J. Freund, *Catal. Today*., 2006, **117**, 6-14.
59 B. Yoon, H. Häkkinen, U. Landman, A. S. Wörz, J. M. Antonietti, S. Abbet, K. Judai and U. Heiz, *Science.*, 2005, **307**, 403-407.
60 C. Ruggiero and P. Hollins, *Surf. Sci.*, 1997, **377-379**, 583-586.
61 J. Kim, E. Samano and B. E. Koel, *J. Phys. Chem. B.*, 2006, **110**, 17512-17517.
62 M. S. Chen, Y. Cai, Z. Yan and D. W. Goodman, *J. Am. Chem. Soc.*, 2006, **128**, 6341-6346.
63 F. Boccuzzi, A. Chiorino, S. Tsubota and M. Haruta, J. Phys. Chem., 1996, **100**, 3625 – 3631.
64 F. Boccuzzi, A. Chiorino, M. Manzoli, P. Lu, T. Akita, S. Ichikawa abd M. Haruta, *J. Catal*., 2001, **202**, 256-267.
65 Y. D. Kim, M. Fischer and G. Gantefor, *Chem. Phys. Lett*., 2003, **377**, 170-176.
66 A. Corma and H. Garcia, *Chem. Soc. Rev*., 2008, **37**, 2096-2126.
67 S. Nishimura, Y. Yakita, M. Katayama, K. Higashimine and K. Ebitani, *Catal. Sci. Technol.*, 2013, **3**, 351-359.
68 S. J. Sun, M. Kohyama, S. Tanaka and S. Takeda, *J. Phys. Chem. A.*, 2012, **116**, 9568-9573.
69 M. Conte, H. Miyamura, S. Kobayashi and V. Chechik, *J. Am.Chem. Soc.*, 2009, **131**, 7189-7196.

**Table Of Contents**

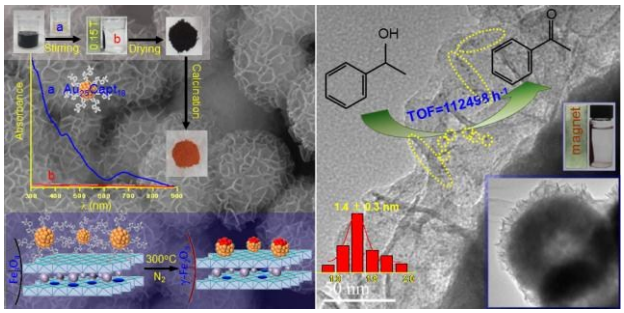


Magnetically recyclable 3D hierarchical hollow nanostructured $Au_{25}$ nanoclusters catalysts assembled by $Au_{25}Capt_{18}$ precursor method exhibit extraordinarily catalytic performance for aerobic oxidation of alcohol by molecular oxygen upon strong $Au_{25}$NCs–LDH–magnetic core synergy.